A Kinetic-Based Model for High-Speed, Monodisperse, Fluid-Particle Flows

Victor Boniou, Rodney O. Fox, Frédérique Laurent

A Kinetic-Based Model for High-Speed, Monodisperse, Fluid–Particle Flows

Victor Boniou[a], Rodney O. Fox[a,b], Frédérique Laurent[b]

[a]*Department of Chemical and Biological Engineering, Iowa State University, Ames, IA 50011-1098, USA*
[b]*Laboratoire EM2C, CNRS, CentraleSupélec, Université Paris-Saclay, 3 rue Joliot-Curie, 91192 Gif-sur-Yvette, France*

Abstract

Three-dimensional (3-D) hyperbolic conservation equations for fully compressible, monodisperse, fluid–particle flows with added mass and fluid-phase pseudoturbulence are proposed. A particle-phase kinetic model is developed that accounts for collisional and frictional terms, as well as added mass and internal energy. Transport equations for 3-D velocity moments up to second order (or total kinetic energy) are closed using a Maxwellian distribution. The resulting two-fluid model is well posed for any fluid–particle material density ratio. The numerical methods associated with the hyperbolic system of equations are designed to fulfill the main features of a compressible two-phase flow solver: capturing of sharp particle fronts, preserving contact discontinuities, and ensuring stability in all flow regimes. This is done by employing a combination of an AUSM$^+$up scheme for the particle phase, and a HLLC scheme for the fluid phase. Stability is obtained by keeping the discrete consistency between spatial fluxes and buoyancy-like terms implying derivatives. Test cases involving a high-speed fluid interacting with heavy/light particles are used to demonstrate that the qualitative behavior of the flow dynamics is captured correctly by the model.

Keywords: fluid–particle flow, kinetic theory of granular flow, hyperbolic quadrature method of moments, added mass, pseudoturbulence

1. Introduction

High-speed flows in the presence of a particle phase occur in numerous natural and industrial problems such as volcanic ash plumes [43], dust explosions [12], or rocket propulsion [10]. The complexity of such multiphase flows stems from the interaction between the shock and the particles, which highly depends on the volume fraction [54]. While dilute mixtures can be approximated with experiments and numerical simulations of isolated particles subject to a shock, the presence of neighboring particles cannot be neglected when their volume fraction increases [32]. In denser mixture, a particle is not only subject to the incident shock wave, but also to shock reflections and expansion waves coming from the other particles and compaction waves transmitted through the granular phase. When the mixture becomes highly dense, the particles are always in contact and the inter-particle interactions become dominant. The proper modeling of granular flows requires to handle these three regimes with an appropriate physical description. Since the pioneering experiments on a gas-shock interaction with particle curtains [44], both numerical and experimental studies have been conducted to give a better description of the shock-induced dispersal of particles. More specifically, experimental studies have been dedicated to the definition of a universal scaling of spread rate with respect to material properties, Mach number, and particle concentration [9, 11, 49]. These works have been followed up by numerical studies to assess new multiphase flow models [27, 32, 38]. More recently, these studies have been extended to hypersonic flows [52] and underwater shocks [2].

In this work, we develop hyperbolic conservation equations for collisional particle flow with added mass and internal energy derived from the kinetic theory of granular flows. For clarity, we consider monodisperse, spherical particles with arbitrary material density and identical physical properties so that only the particle velocity distribution function is needed in the kinetic model. In most applications, the fluid will either be a gas interacting with high-density

Email addresses: boniouv@iastate.edu (Victor Boniou), rofox@iastate.edu (Rodney O. Fox), frederique.laurent@centralesupelec.fr (Frédérique Laurent)

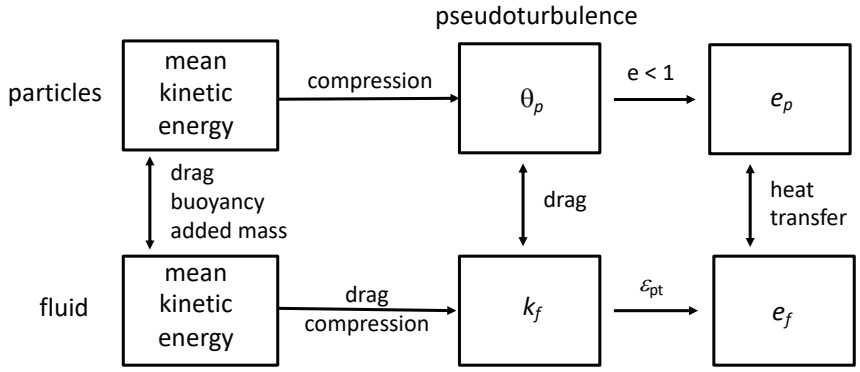

Figure 1: Energy flow in fluid–particle, two-fluid model for monodisperse particles. Spatially uncorrelated particle motion is measured by Θ_p, while particle-scale, fluid-phase, fluctuating kinetic energy is measured by k_f. The internal energies are e_p and e_f. Inelastic collisions transform Θ_p into an increase in e_p. Pseudoturbulent dissipation ε_{pt} transform k_f into an increase in e_f. At each scale, the phases are coupled through drag and heat transfer, and a drag correlation and the Nusselt number are important inputs to the two-fluid model.

solid particles or a liquid interacting with low-density particles (e.g., bubbles). For simplicity, we assume that the particle material density remains constant, which implies that the particle volume is constant. However, the extension to allow for the particle material density (and hence the volume) to vary with the fluid pressure is straightforward provided that the particle Stokes number for such cases is small (i.e., bubbly flow).

In the proposed two-fluid model, the particle-phase equations are coupled with modified Euler equations for the fluid phase, including pseudoturbulent kinetic energy (PTKE) [46]. Due to the high-speed nature of the flow, viscous terms are neglected but can easily be included when needed [30]. Details on the derivation of the forces and fluxes in the monodisperse two-fluid model can be found in prior work [16, 20, 31]. The fluid phase is treated as inviscid with coupling terms discussed in [20], and the stiffened gas equation of state is used for the fluid pressure. The particle phase with added mass and internal energy is treated as inelastic and inviscid, and a frictional pressure term is added to handle dense cases. Particle velocity moments up to second order (total kinetic energy) are included, which is sufficient for collisional flows [15]. The model then accounts for conservation of mass, momentum and total energy for both phases.

The diagram in fig. 1 provides a schematic on how kinetic energy is distributed in the fluid–particle flow. The mean kinetic energy is found from the phasic velocities appearing in the momentum balances. Due to their finite size, particles have wakes produced by the slip velocity whose characteristic length scale is proportional to the particle diameter. These wakes interact with individual particles to generate uncorrelated velocity fluctuations measured by the granular temperature [15]. This kinetic energy is dissipated to yet smaller scales to modify the internal energy of both phases. In the absence of body forces (e.g., gravity), the total energy of the two phases is a conserved quantity, and it must be treated as such in the two-fluid model. In a closed system, the total energy at equilibrium will reside in the internal energies, such that the thermodynamics temperature of both phases are equal.

The remainder of this paper is organized as follows. In section 2, we present the balance equations for the fluid phase developed in [20]. In section 3, a kinetic model for the particles is developed, leading to a hyperbolic two-fluid model very similar to the one in [20]. Then, in section 4, we present a robust numerical algorithm for solving the model equations for arbitrary material-density ratios ranging from bubbly liquids to gas–particle flows. Section 5 is devoted to 1-D numerical examples using flow conditions taken from the literature. Finally, in section 6, conclusions are drawn and possible extensions to low-Mach-number and combusting flows are discussed.

2. Fluid-phase governing equations for compressible fluid–particle flows

The principal objective in this section is to review how added mass, internal energy, and PKTE are treated for the fluid phase based on the hyperbolic two-fluid model from [17, 20].

2.1. Definitions

The fluid material density is denoted by ρ_f, and the solids material density (assumed to be constant) is ρ_p. The fluid- and particle-phase velocities are $\mathbf{u}_f$ and $\mathbf{u}_p$, respectively. The total energies of the fluid and particle phases are denoted as E_f and E_p, respectively. The total energy is made up of kinetic + internal energies. We denote the former for each phase as K_f and K_p, and the latter as e_f and e_p. Hence,

$$E_f = K_f + e_f, \quad E_p = K_p + e_p. \tag{1}$$

The kinetic energy is further divided into mean and fluctuating components (see fig. 1):

$$K_f = \frac{1}{2}u_f^2 + k_f, \quad K_p = \frac{1}{2}u_p^2 + \frac{3}{2}\Theta_p. \tag{2}$$

Here, $u^2 = \mathbf{u}\cdot\mathbf{u}$, k_f is the PTKE, and Θ_p is the granular temperature. The former represents fluid-velocity fluctuations due to finite-size particles, and the square root of the latter represents the velocity magnitude of individual particles relative to $\mathbf{u}_p$. In the two-fluid model, the total energy of both phases is conserved. For the fluid phase, it is convenient to solve transport equations for E_f and k_f, and to find e_f from eq. (1). In contrast, for the particle phase, the kinetic description leads naturally to transport equations for K_p and e_p, and then Θ_p is found from eq. (2). In any case, the thermodynamic temperatures T_f and T_p are found from the internal energies e_f and e_p, respectively.

2.2. Added-mass continuity equation

In our modeling approach [8, 20], added mass is handled by assigning a fraction of the fluid phase surrounding a particle to move with the velocity of the particle phase $\mathbf{u}_p$. In the context of two-fluid models, we define $\alpha_p^\star = \alpha_p + \alpha_a$ where α_a is the volume fraction of the added-mass phase while α_p is the particle-phase volume fraction. In the absence of particles, both α_p and α_a are null. It then follows that $\alpha_f^\star = \alpha_f - \alpha_a$ where α_f is the fluid-phase volume fraction. The mass balances for pure particle and added-mass phases are, respectively,

$$\partial_t \rho_p \alpha_p + \partial_{\mathbf{x}} \cdot \rho_p \alpha_p \mathbf{u}_p = 0 \tag{3}$$

and

$$\partial_t \rho_f \alpha_a + \partial_{\mathbf{x}} \cdot \rho_f \alpha_a \mathbf{u}_p = S_a \tag{4}$$

where S_a is a mass-transfer rate from the fluid phase to the added-mass phase. If we rewrite the added-mass volume fraction as $\alpha_a = c_m \alpha_f \alpha_p$ where $0 < c_m < 1$ is the added-mass coefficient with equilibrium value $c_m^\star$, then S_a can be modeled using

$$S_a = \frac{1}{\tau_a}\rho_f \alpha_f \alpha_p (c_m^\star - c_m). \tag{5}$$

The default value of $c_m^\star$ for steady, incompressible flow is set to

$$c_m^\star = \frac{1}{2}\min(1 + 2\alpha_p, 2). \tag{6}$$

The time scale for relaxation towards equilibrium τ_a is assumed to be proportional to the time scale for single-particle drag τ_p.

Physically, the added-mass phase represents the fluid surrounding a particle [8, 20]. Thus, heat and mass transfer to (from) the particle phase from (to) the fluid phase pass through the added-mass phase. For simplicity, here we will assume that the internal energy of the particle + added mass (denoted by e_p) is uniform in the particle, leading to a single temperature T_p.[1] This assumption is compatible with [27], and is used to define the temperature difference $T_p - T_f$ that drives heat transfer between the two phases. As usual, the volume fractions are non-negative with $\alpha_p + \alpha_f = 1$ and $\alpha_p^\star + \alpha_f^\star = 1$.

[1] The effective heat capacity of the particle + added mass can be approximated using the heat capacities of the fluid and solid weighted by α_a and α_p, respectively.

2.3. Continuous fluid-phase mass, momentum, total energy, and PTKE balances

In conservative form, the continuous fluid phase is governed by mass, momentum, total-energy, and PTKE balances (neglecting gravity for simplicity) [20]:

$$\partial_t \rho_f \alpha_f^\star + \partial_{\mathbf{x}} \cdot \rho_f \alpha_f^\star \mathbf{u}_f = -S_a \tag{7}$$

$$\partial_t \rho_f \alpha_f^\star \mathbf{u}_f + \partial_{\mathbf{x}} \cdot (\rho_f \alpha_f^\star \mathbf{u}_f \otimes \mathbf{u}_f + \hat{p}_f \mathbf{I} + \mathbf{P}_{pfp}) = \mathbf{D} + \alpha_p^\star (\partial_{\mathbf{x}} \hat{p}_f + \mathbf{F}_{pf}) + \partial_{\mathbf{x}} \cdot \mathbf{P}_{pfp} - \mathbf{S}_{gp} \tag{8}$$

$$\partial_t \rho_f \alpha_f^\star E_f + \partial_{\mathbf{x}} \cdot (\rho_f \alpha_f^\star \mathbf{u}_f E_f + \alpha_f^\star \mathbf{u}_f \hat{p}_f + \alpha_p^\star \mathbf{u}_p \hat{p}_f + \mathbf{u}_p \cdot \mathbf{P}_{pfp}) = D_E + \alpha_p^\star \mathbf{u}_p \cdot (\partial_{\mathbf{x}} \hat{p}_f + \mathbf{F}_{pf}) + \mathbf{u}_p \cdot (\partial_{\mathbf{x}} \cdot \mathbf{P}_{pfp}) + H_{pf} - S_E \tag{9}$$

$$\partial_t \rho_f \alpha_f^\star k_f + \partial_{\mathbf{x}} \cdot \rho_f \alpha_f^\star \mathbf{u}_f k_f + \frac{2}{3} \rho_f \alpha_f^\star k_f \partial_{\mathbf{x}} \cdot \mathbf{u}_f = D_{PT} - \rho_e \alpha_p^\star \frac{C_f}{\tau_p} k_f \tag{10}$$

where $\hat{p}_f = p_f + \frac{2}{3}\rho_f k_f$ is the modified fluid pressure, and $\mathbf{D}$, D_{PT}, and D_E represent drag exchange with the particle phase. The slip velocity is denoted by $\mathbf{u}_{pf} = \mathbf{u}_p - \mathbf{u}_f$. The fluid pressure is found from an equation of state. In this work, we will use the stiffened-gas law:

$$p_f = (\gamma_f - 1)\rho_f \left(E_f - K_f\right) - \gamma_f p_{\infty,f} = (\gamma_f - 1)\rho_f e_f - \gamma_f p_{\infty,f} \tag{11}$$

where γ_f is the heat-capacity ratio. For an ideal gas, the reference pressure $p_{\infty,f}$ is set to 0, leading to the well-known ideal-gas law. In liquids, $p_{\infty,f} > 0$ is used to control the speed of sound. In the total energy balance, H_{pf} represents convective heat transfer from the particle phase due to the temperature difference [27].

For monodisperse particles, the drag-exchange terms are defined by

$$\mathbf{D} = \frac{\rho_e \alpha_p^\star}{\tau_p} \mathbf{u}_{pf}, \quad D_E = \frac{\rho_e \alpha_p^\star}{\tau_p} [\mathbf{u}_p \cdot \mathbf{u}_{pf} + 3a\Theta_p - 2(1-a)k_f], \quad D_{PT} = \frac{\rho_e \alpha_p^\star}{\tau_p} [u_{pf}^2 + 3a\Theta_p - 2(1-a)k_f] \tag{12}$$

where ρ_e is the effective particle density, with $\rho_e \alpha_p^\star + \rho_f \alpha_f^\star = \rho_p \alpha_p + \rho_f \alpha_f$. The parameter a depends on the material densities, and is modeled as

$$a = \frac{\rho_p + \rho_f a_{min}}{\rho_p + \rho_f} \tag{13}$$

where $a_{min} = 0.5$ determines the steady-state ratio Θ_p / k_f for gas bubbles in a liquid (i.e., $\rho_p / \rho_f \ll 1$). Heavy particles in a gas correspond to $a \lessapprox 1$. Physically, $D_{PT} \geq 0$ represents kinetic energy lost from the particle phase to produce PTKE in the fluid phase, and PTKE dissipates to heat the fluid phase. For shock–particle interactions, the drag time scale τ_p is an important parameter, depending on the particle Reynolds number, Mach number, and volume fraction.

The parameter C_f in eq. (10) controls the rate of dissipation of PTKE into internal energy in the fluid phase [46]. Here, we will use the correlation from PR-DNS with frozen particles [39]:

$$C_f^{-1} = \alpha_p [1 + 1.25\alpha_f^3 \exp(-\alpha_p \alpha_f^{1/2} Re_p^{1/2})], \tag{14}$$

where the particle Reynolds number is

$$Re_p = \frac{\rho_f d_p u_{pf}}{\mu_f}, \tag{15}$$

and μ_f is the fluid-phase viscosity (which depends on T_f). At a steady state with constant u_{pf}, we then find

$$\frac{k_f}{u_{pf}^2} \to C_f^{-1}, \quad \Theta_p \to \frac{2(1-a)}{3a} k_f. \tag{16}$$

The correlation in eq. (14) is valid for uniform α_p. When k_f is transported from a uniform region to a very dilute region (e.g., behind a particle curtain), C_f from eq. (14) can be much too large. Possible alternatives are to replace, in dilute regions, C_f / τ_p by $C_f^* k_f^{1/2} / d_p$ where C_f^* is a constant of order one, or to solve a transport equation for pseudoturbulence frequency ω_{pt} [17, 46].

The final terms on the right-hand sides of eq. (7)–eq. (9) represent exchanges between the continuous fluid phase

and the added-mass phase [27].[2] They are modeled for mass by eq. (5), for momentum by

$$\mathbf{S}_{gp} = \max(S_a, 0)\,\mathbf{u}_f + \min(S_a, 0)\,\mathbf{u}_p \tag{17}$$

and for the total energy by

$$S_E = \max(S_a, 0)\,E_f + \min(S_a, 0)\,E_p. \tag{18}$$

In words, if S_a is positive, mass, fluid-phase momentum and total energy are transferred from the continuous phase to the added-mass phase, while for negative S_a the transfer is in the opposite direction.

The slip-pressure tensor $\mathbf{R}$ and momentum exchange term $\mathbf{F}_{pf}$ arise due to finite-size particles [20], and are the same as when added mass is neglected. For a monodisperse system, they were derived from kinetic theory [16] as

$$\begin{aligned} \mathbf{R} &= \frac{1}{5}u_{pf}^2\mathbf{I} + \frac{2}{5}\mathbf{u}_{pf}\otimes\mathbf{u}_{pf} \\ \mathbf{F}_{pf} &= \mathbf{R}\cdot\partial_{\mathbf{x}}\rho_f - \frac{2}{3}\rho_f tr(\mathbf{\Gamma})\,\mathbf{u}_{pf} - \frac{4}{5}\rho_f\mathbf{S}\cdot\mathbf{u}_{pf} \end{aligned} \tag{19}$$

where the deformation rate tensor is $\mathbf{\Gamma} = \frac{1}{2}\left[\partial_{\mathbf{x}}\mathbf{u}_f + (\partial_{\mathbf{x}}\mathbf{u}_f)^t\right]$ and $\mathbf{S} = \mathbf{\Gamma} - \frac{1}{3}tr(\mathbf{\Gamma})\mathbf{I}$. The term $\mathbf{R}\cdot\partial_{\mathbf{x}}\rho_f$ can be important when strong shocks are present, i.e., where the fluid density changes rapidly. The second term in $\mathbf{F}_{pf}$ modifies the fluid drag when $0 < |\partial_{\mathbf{x}}\cdot\mathbf{u}_f|$, while the third term represents lift. The latter was derived considering only mean gradients of density and velocity in a compressible flow [16], and should be replaced by a lift model accounting for the particle Reynolds number [27]. In practice, $\mathbf{F}_{pf}$ can have the same order of magnitude as the buoyancy force ($\partial_{\mathbf{x}}\hat{p}_f$). The latter must be included in moderately dense and dense flows in order to get the correct eigenvalues for the fluid-phase spatial flux. Note that $tr(\mathbf{R}) = u_{pf}^2$.

The particle–fluid–particle (*pfp*) pressure tensor described in [20] can be modeled as

$$\mathbf{P}_{pfp} = C_{pfp}\rho_f\alpha_p^\star\mathbf{R} \tag{20}$$

with $C_{pfp} = c_m^\star$ ensuring hyperbolicity when $\rho_p \ll \rho_f$ (e.g., bubbly flows). Note that in eq. (8), the $\mathbf{P}_{pfp}$ term can be moved inside the flux term on the left-hand side. Thus, the slip-pressure tensor only modifies the particle-phase pressure tensor. We should note that this term has physical relevance for freely moving particles, i.e., below the close-packed limit. However, above close packing, its contribution will be very small compared to fluid drag. More generally, $tr(\mathbf{P}_{pfp})$ is usually very small compared to the fluid pressure p_f, and therefore has essentially no effect on the fluid-phase speed of sound. Nonetheless, it is important for the particle phase, particularly in dilute cases, and in high-speed flows with a large slip velocity or steep volume-fraction gradient (e.g., a shock hitting a particle curtain).

Recently [53], the *pfp* stress tensor $\mathbf{\Sigma}_{pfp}$ ($= -\mathbf{P}_{pfp}$) has been computed for fixed particles ($\Theta_p = 0$) in an incompressible fluid. These authors found that the *pfp*-pressure tensor has the form

$$\mathbf{P}_{pfp} = \rho_f\alpha_p^\star\left[B_1(\alpha_p, Re_p)\,u_{pf}^2\mathbf{I} + B_2(\alpha_p, Re_p)\,\mathbf{u}_{pf}\otimes\mathbf{u}_{pf}\right] \tag{21}$$

with positive trace, and they provide correlations for B_1 and B_2 over limited ranges of α_p and Re_p. For example, they find that B_1 has a weak dependence on α_p (i.e., $-0.01\ln\alpha_p$) and B_2 is nearly independent of α_p. More generally, the tensor form in eq. (21) is unique for systems without macroscopic gradients [53]. It may therefore be reasonable to use B_1 and B_2 in eq. (21) to redefine the coefficients in $\mathbf{R}$ (i.e., replacing 1/5 and 2/5, respectively) such that C_{pfp} in eq. (20) is defined by enforcing $tr(\mathbf{R}) = u_{pf}^2$. In any case, for one-dimensional (1-D) flows, only $tr(\mathbf{P}_{pfp}) = C_{pfp}\rho_f\alpha_p^\star u_{pf}^2$ is required in the 1-D model.

In summary, the inclusion of added mass requires an additional continuity equation eq. (4), along with source terms to model changes in the added-mass volume fraction, momentum and total energy. The total mass of the particle + added-mass phase can be expressed as

$$\rho_e\alpha_p^\star = \rho_p\alpha_p + \rho_f\alpha_a, \tag{22}$$

which defines the effective density ρ_e. In the next section, we develop a kinetic model for monodisperse particles with

[2] These terms correspond to the terms involving $\dot{M}$ in [27].

added mass and internal energy. This model will be used to find balance equations for the particle-phase variables $\rho_e\alpha_p^\star$, $\rho_e\alpha_p^\star\mathbf{u}_p$, $\rho_e\alpha_p^\star K_p$, and $\rho_e\alpha_p^\star e_p$. In addition, the conserved variable $\rho_p\alpha_p$, governed by eq. (3), is needed to determine ρ_f when the fluid is compressible.

3. Kinetic model for monodisperse particles with added mass

In order to account for the particle pressure due to collisions and friction in a simplified, but accurate, manner, we use a kinetic model for the particles [37]. At the kinetic level, individual particles with different velocities $\mathbf{u}$ are represented by a distribution function $f(t, \mathbf{x}, \mathbf{u}, e)$, the moments of which contain information such as the mass, momentum and kinetic energy of the particle phase.[3] The internal energy of a particle e moves with velocity $\mathbf{u}$, and is accounted for as an internal variable [37].[4] Here, we close the moment equations at the level of the particle-phase kinetic energy, which is sufficient for describing collisional and/or low-Stokes-number flows. However, the kinetic model can be used to find transport equations for higher-order moments, such as for the anisotropic Gaussian model [30, 51] or quadrature-based moment methods [19], that are needed for weakly collisional or collision-less flows.

3.1. Kinetic model

The proposed kinetic model for the distribution function has the following form:

$$\partial_t f + \partial_{\mathbf{x}} \cdot \left(\mathbf{u} f - P_p \frac{\partial f}{\partial \mathbf{u}} \right) + \frac{\partial}{\partial \mathbf{u}} \cdot \left[\mathbf{A}_u f - \frac{1}{\rho_e} (\partial_{\mathbf{x}} \hat{p}_f + \mathbf{F}_{pf}) f - \frac{1}{\rho_e \alpha_p^\star} (\partial_{\mathbf{x}} \cdot \mathbf{P}_{pfp}) f \right] + \frac{\partial}{\partial e}(A_e f) = \frac{\partial^2}{\partial \mathbf{u} \partial \mathbf{u}} : \mathbf{B}_u f + C + F + S. \quad (23)$$

Below, we define separately each of the terms appearing in this kinetic equation. In words, the distribution function f is proportional to the average number of particles at space–time location $(t, \mathbf{x})$ with phase-space properties $(\mathbf{u}, e)$. Thus, at the particle level, each particle has its own velocity $\mathbf{u}$ and internal energy e, but otherwise the particle properties are identical. In eq. (23), we treat $\mathbf{P}_{pfp}$ and $\mathbf{F}_{pf}$ as independent of $\mathbf{u}$; however, this is not a requirement for deriving the two-fluid model.

In what follows, the dependence of functions on $(t, \mathbf{x})$ is dropped, and the following notation is used:

$$\langle \varphi \rangle = \int \varphi(\mathbf{u}, e) f(\mathbf{u}, e) \, \mathrm{d}\mathbf{u} \, \mathrm{d}e \quad (24)$$

for any function φ. To account for the added mass, the distribution function is scaled such that the conserved particle-phase variables (i.e., mass, momentum, internal energy, kinetic energy) are defined, respectively, by

$$\langle 1 \rangle = \rho_e \alpha_p^\star, \quad \langle \mathbf{u} \rangle = \rho_e \alpha_p^\star \mathbf{u}_p, \quad \langle \frac{1}{2} \mathbf{u}^2 \rangle = \rho_e \alpha_p^\star K_p, \quad \langle e \rangle = \rho_e \alpha_p^\star e_p. \quad (25)$$

Strictly speaking, this scaling requires that $\rho_p + \rho_f c_m \alpha_f$ be the same for all particles (e.g., $c_m = 0$) so that the particle mass + added mass is constant. Otherwise, one must account for a distribution of particle masses as must be done for polydisperse particles [31, 37]. In practice, we can ignore this detail as long as the resulting balance equations conserve mass, momentum and energy.

3.1.1. Transfer terms

In eq. (23), for the fluid-drag term, the acceleration vector $\mathbf{A}_u$ has the form

$$\mathbf{A}_u = \frac{\mathbf{u}_f - \mathbf{u}}{\tau_p} \quad (26)$$

[3] In this context, "phase balance" means a balance over the ensemble of all particles. Thus, information concerning individual particles is lost, but classical conservation of mass, momentum and energy still hold.

[4] When needed, the chemical composition of the particles is handled in the same manner as internal energy.

where τ_p is the drag time scale that depends on α_p and $\mathbf{u}_{pf}$:

$$\tau_p = \frac{4\rho_e d_p^2}{3\mu_f C_D Re_p}. \tag{27}$$

Here, d_p is the particle diameter and C_D is a drag coefficient that depends on the particle Reynolds number[5] and other dimensionless parameters such as the Mach number and volume fraction. For Stokes flow, which is valid for very small particles and $\alpha_f = 1$, $C_D Re_p = 24$.

The term in eq. (23) involving A_e accounts for exchange of particle-phase internal energy e_p with the fluid phase due to the temperature difference. Denoting the particle temperature by T, which is in a one-to-one relation with e, we can define this term by

$$A_e = \frac{6\lambda_f Nu}{\rho_e d_p^2}(T_f - T) \qquad \Longrightarrow \qquad H_{pf} = -\langle A_e \rangle = \frac{6\alpha_p^\star \lambda_f Nu}{d_p^2}(T_p - T_f) \tag{28}$$

where the phase temperatures are found from their internal energies. Hereinafter, for simplicity, we will take the heat capacities as constant such that

$$T_f = \frac{\gamma_f e_f}{C_{p,f}}, \qquad T = \frac{e}{C_{V,p}}, \qquad T_p = \frac{e_p}{C_{V,p}}. \tag{29}$$

This assumption will be valid as long as the temperatures do not vary too much. The Gunn correlation [25] for the Nusselt number (Nu) is given in [27] and table 2, and λ_f is the fluid-phase thermal conductivity.

The velocity diffusion term on the right-hand side of eq. (23) with coefficient matrix

$$\mathbf{B}_u = \frac{1-a}{\tau_p}\left((\mathbf{u} - \mathbf{u}_p) \otimes (\mathbf{u} - \mathbf{u}_p) + \frac{2}{3}k_f \mathbf{I}\right) \qquad \Longrightarrow \qquad \langle tr(\mathbf{B}_u) \rangle = \rho_e \alpha_p^\star \frac{1-a}{\tau_p}\left(3\Theta_p + 2k_f\right) \tag{30}$$

is due to fluid-phase PTKE accelerating the particles relative to their mean velocity with drag timescale τ_p. In $\langle tr(\mathbf{B}_u) \rangle$, the total fluctuating energy in both phases is $3\Theta_p + 2k_f$, so that the parameter a controls the amount transferred to the particles. If PTKE anisotropy were accounted for in the model [17], $2k_f/3$ would be replaced by the PTKE Reynolds stress tensor. For gas–particle flows, a is nearly unity and hence $\mathbf{B}_u$ is very small, or even negligible.

3.1.2. Added-mass terms

For clarity, here we will assume that particle-mass fluctuations due to added-mass exchange are small enough to be neglected. Thus, eq. (23) has the same form as without added mass, but with the exchange term $S(\mathbf{u}, e)$ on the right-hand side. To be consistent with the fluid-phase balances, we require that this exchange term have the following integral properties:

$$\int S(\mathbf{u}, e)\, \mathrm{d}\mathbf{u}\, \mathrm{d}e = S_a, \quad \int e\, S(\mathbf{u}, e)\, \mathrm{d}\mathbf{u}\, \mathrm{d}e = S_e, \quad \int \mathbf{u} S(\mathbf{u}, e)\, \mathrm{d}\mathbf{u}\, \mathrm{d}e = \mathbf{S}_{gp}, \quad \int \frac{1}{2}u^2 S(\mathbf{u}, e)\, \mathrm{d}\mathbf{u}\, \mathrm{d}e = S_K \tag{31}$$

where the kinetic-energy source term is

$$S_K = \max(S_a, 0)\, K_f + \min(S_a, 0)\, K_p, \tag{32}$$

the internal-energy source term is

$$S_e = \max(S_a, 0)\, e_f + \min(S_a, 0)\, e_p, \tag{33}$$

and the other source terms on the right-hand sides are given in section 2.2. These properties ensure conservation of mass, internal energy, momentum, and kinetic energy for the sum of the two phases. Note that $S_E = S_K + S_e$ as expected.

[5] In the usual definition of Re_p, the slip velocity $\mathbf{v}_{pf}$ is defined in the absence of added mass. As shown in [20], the slip velocities are related by $\alpha_f \mathbf{v}_{pf} = \alpha_f^\star \mathbf{u}_{pf}$. The slip velocity with added mass is larger because part of the fluid moves with the particle velocity $\mathbf{u}_p$. However, drag models in the literature are based on v_{pf}, so that τ_p in eq. (27) can be multiplied by $\alpha_f/\alpha_f^\star$ to recover the correct drag force.

A simple model for $S(\mathbf{u}, e)$ that satisfies these constraints is

$$S(\mathbf{u}, e) = C_\xi f + C_u \frac{\partial}{\partial e}(e - e_f) f + C_u \frac{\partial}{\partial \mathbf{u}} \cdot (\mathbf{u} - \mathbf{u}_f) f + \frac{1}{2} C_u \frac{\partial^2}{\partial \mathbf{u} \partial \mathbf{u}} : \mathbf{D}_u f \tag{34}$$

with parameters

$$C_\xi = \frac{S_a}{\rho_e \alpha_p^\star}, \quad C_u = \frac{1}{2}(C_\xi + |C_\xi|), \tag{35}$$

and velocity diffusion matrix

$$\mathbf{D}_u = (\mathbf{u} - \mathbf{u}_f) \otimes (\mathbf{u} - \mathbf{u}_f) + \frac{2}{3} k_f \mathbf{I}. \tag{36}$$

The final term in eq. (36) represents an isotropic model for the PTKE Reynolds stress tensor. Thus, if the PTKE model is extended to include the full stress tensor, it should be used in place of the isotropic model.

Note that $C_u = 0$ when $S_a \leq 0$ (i.e., when added mass is transferred to the gas phase), otherwise $C_u = C_\xi$. The first term on the right-hand side of eq. (34) represents the change in added mass, the second is transfer of internal energy, the third is acceleration due to change in added mass, and the fourth is change in kinetic energy due to change in added mass; all of which occur with constant solid particle mass, i.e., only the added mass of fluid changes.

3.1.3. Pressure terms

The particle-phase pressure $P_p = P_c + P_f$ depends on the velocity moments up to second order [16], and is the sum of a collisional component:

$$P_c = 2(1 + e_c)\alpha_p g_0 \Theta_p, \quad g_0 = \frac{1 + \alpha_f}{2\alpha_f^3} \tag{37}$$

where e_c is the coefficient of restitution; and a frictional component, modeled here as

$$P_f = \frac{p_f \alpha_p g_0}{\rho_e \alpha_p^\star} \frac{1}{2} \left[1 + \tanh\left(\frac{\alpha_p - \alpha_{max}}{\Delta_f} \right) \right] \tag{38}$$

where $\alpha_{max} = 0.63$ is the closed-packed limit and $\Delta_f = 0.01$ is chosen to have a sharp transition at α_{max}. The parameter p_f fixes the speed of sound in the particle phase above the closed-packed limit. The functional form of eq. (38) causes P_f to rapidly increase from zero near $\alpha_p = \alpha_{max}$. In general, the functional form for P_f must ensure that the frictional pressure increases monotonely with volume fraction, i.e., $d\rho_e \alpha_p^\star P_f / d\alpha_p > 0$. For $\alpha_p < \alpha_{max}$, the particle-phase speed of sound scales with $\sqrt{3\Theta_p}$. Finally, note that added mass plays no role in $\rho_e \alpha_p^\star P_f$ because the particles are in contact. Other forms for P_c that account for velocity correlations between colliding particles are also available [29]. Here, for clarity, when the particle pressure depends on both α_p and Θ_p, we refer to it as collisional; otherwise, when it depends only on α_p, we refer to it as frictional.

3.1.4. Collisional source term

The microscale (particle-level) model for binary collisions has the following properties. Let $(\mathbf{u}, e)_1, (\mathbf{u}, e)_2$ be the particle velocities and internal energies before a collision, and $(\mathbf{u}', e')_1, (\mathbf{u}', e')_2$ be the values after collision. Then, for monodisperse particles with equal (and constant) masses, we have the following four identities:

$$\begin{aligned} \mathbf{u}_1' + \mathbf{u}_2' &= \mathbf{u}_1 + \mathbf{u}_2 \\ u_1'^2 + u_2'^2 &= e_c^2(u_1^2 + u_2^2) \\ u_1'^2 + u_2'^2 + e_1' + e_2' &= u_1^2 + u_2^2 + e_1 + e_2 \\ e_1' - e_2' &= e_1 - e_2 \end{aligned} \tag{39}$$

corresponding, respectively, to conservation of momentum, kinetic energy, total energy, and equal distribution of change in internal energy. The first three come from Newton's laws of motion, while the fourth comes from the assumption that the change in internal energy for each particle is the same, regardless of its velocity or internal energy. It is straightforward to show that $e_1' - e_1 = \frac{1}{2}(1 - e_c^2)(u_1^2 + u_2^2)$, i.e., the increase in internal energy is proportional to

the kinetic energy of the particles before collision. Because collisions are Galilean invariant, a frame of reference with zero mean velocity can be chosen such that $\mathbf{u}_1$ and $\mathbf{u}_2$ correspond to fluctuating velocities. Hence, the change in internal energy of the particle phase e_p is proportional to Θ_p.

The collisional source term C on the right-hand side of eq. (23) is modeled using the inelastic BGK closure [4, 42], extended to include internal energy. Using eq. (39), the particle-phase kinetic-energy balance requires $\langle \mathbf{u}^2 C \rangle \leq 0$, and the equality holds for elastic collisions ($e_c = 1$). In general, the inelastic BGK model can be written as

$$C(\mathbf{u}, e) = \frac{\rho_e \alpha_p^\star f_G(\mathbf{u}, e) - f(\mathbf{u}, e)}{\tau_c} \tag{40}$$

where f_G is a Gaussian distribution with the same mean velocity as f (i.e., $\langle \mathbf{u} f_G \rangle = \mathbf{u}_p$) and τ_c is the collision time that depends on α_p and Θ_p:

$$\tau_c = \frac{d_p \sqrt{\pi}}{12 \alpha_p g_0 \Theta_p^{1/2}}. \tag{41}$$

For inelastic collisions ($e_c < 1$), the covariance matrix of f_G depends on $\omega = (1 + e_c)/2$ [37], as well as its mean value in e, which is $\langle e f_G \rangle = e_p + (1 - e_c^2)\Theta_p$. This leads to the collisional contribution to the particle-phase heating term:

$$\langle eC \rangle = -\left. \partial_t \rho_e \alpha_p^\star K_p \right|_c = \rho_e \alpha_p^\star \frac{(1 - e_c^2)}{\tau_c} \Theta_p. \tag{42}$$

Although they are not needed in this work, the identities in eq. (39) also fix $\langle e^2 C \rangle$ and $\langle e\mathbf{u}C \rangle$, and hence the corresponding terms in the covariance matrix of f_G.

3.1.5. Frictional source term and other force terms

The frictional source term F is applicable to dense flows with sustained contacts. Physically, the sole purpose of F is to drive the granular temperature Θ_p to a negligible value when $\alpha_p > \alpha_{max}$, thereby producing particle-phase internal energy e_p such that the total energy E_p is conserved. The frictional model used in this work is

$$F(\mathbf{u}, e) = \frac{\rho_e \alpha_p^\star \delta(\mathbf{u} - \mathbf{u}_p)\delta(e - e_p - \Theta_p) - f(\mathbf{u}, e)}{\tau_f} \tag{43}$$

where τ_f is a time scale that depends on τ_c and $\partial_{\mathbf{x}} \cdot \mathbf{u}_p$:

$$\tau_f = \frac{2 c_f}{\max(|\partial_{\mathbf{x}} \cdot \mathbf{u}_p|, 1/\tau_c)} \left[1 + \tanh\left(\frac{\alpha_p - \alpha_{max}}{\Delta_f} \right) \right]^{-1}. \tag{44}$$

Here, $c_f = 0.01$ controls the frictional time scale above close packing. The τ_c dependence makes τ_f very small when $\alpha_p > \alpha_{max}$. The $|\partial_{\mathbf{x}} \cdot \mathbf{u}_p|$ dependence attempts to capture the effect of relative particle motion under such conditions (i.e., in the absence of deformation there is no friction). The frictional contribution to the particle-phase heating term is

$$\langle eF \rangle = -\left. \partial_t \rho_e \alpha_p^\star K_p \right|_f = \rho_e \alpha_p^\star \frac{1}{\tau_f} \Theta_p. \tag{45}$$

In any case, the primary purpose of the frictional model is to drive Θ_p quickly to zero above close packing.

The Archimedes force ($\partial_{\mathbf{x}} \hat{p}_f$) depends on the fluid-pressure gradient, and $\mathbf{F}_{pf}$ and $\mathbf{P}_{pfp}$ are defined as in eq. (19) and eq. (20). Compared to the full kinetic-theory expression for hard-sphere collisions, the main simplification in eq. (23) is the treatment of collisional pressure. In the full model for hard spheres, the collisional pressure depends on a complicated integral with respect to the two-particle velocity distribution function [16].

3.2. Moment equations

3.2.1. Internal-energy moments

Only two moments involving internal energy are needed for closure: e_p and the flux

$$\langle e\mathbf{u}\rangle = \int e\mathbf{u} f\left(\mathbf{u}, e\right)\, \mathrm{d}\mathbf{u}\, \mathrm{d}e. \tag{46}$$

Consistent with [27], we use the closure $\langle e\mathbf{u}\rangle = \rho_e \alpha_p^\star e_p \mathbf{u}_p$. In fact, coherently with the use of only zero- and first-order moments in e, we assume that $f(\mathbf{u}, e) = f(\mathbf{u})\delta(e - e_p)$; however, including a term for conduction in low-speed granular flows is also possible [3, 29]. The kinetic model in eq. (23) yields the balance equation for particle-phase internal energy:

$$\partial_t \rho_e \alpha_p^\star e_p + \partial_{\mathbf{x}} \cdot \rho_e \alpha_p^\star e_p \mathbf{u}_p = -H_{pf} + \langle eC\rangle + \langle eF\rangle + S_e. \tag{47}$$

The collisional and frictional terms, $\langle eC\rangle$ and $\langle eF\rangle$, are strictly non-negative [27]. The particle-phase heating rate is given by

$$H_p = \langle eC\rangle + \langle eF\rangle = \rho_e \alpha_p^\star \left[\frac{1}{\tau_c}(1 - e_c^2) + \frac{1}{\tau_f}\right]\Theta_p \tag{48}$$

where the collision time τ_c is defined in eq. (41) and the frictional time scale τ_f is defined in eq. (44).

3.2.2. Velocity moments

The velocity moment of integer order $l = i + j + k$ is defined by[6]

$$M^l_{i,j,k} = \int u^i v^j w^k f\left(\mathbf{u}, e\right)\, \mathrm{d}\mathbf{u}\, \mathrm{d}e = \int u^i v^j w^k f\left(\mathbf{u}\right)\, \mathrm{d}\mathbf{u} = \langle u^i v^j w^k\rangle \tag{49}$$

where the vector $\mathbf{u} = (u, v, w)^t$ corresponds to the velocity components in directions $\mathbf{x} = (x, y, z)^t$. The lower-order moments have a physical interpretation. For example,

$$M^0 = \rho_e \alpha_p^\star \tag{50}$$

is the mass of the particle + added-mass phase, and the vector

$$\mathbf{M}^1 = (M_{1,0,0}, M_{0,1,0}, M_{0,0,1})^t = \rho_e \alpha_p^\star \mathbf{u}_p \tag{51}$$

with mean velocity $\mathbf{u}_p = (u_p, v_p, w_p)^t$ is its momentum. The non-negative, symmetric, second-order tensor $\mathbf{M}^2$ is the total-energy tensor:

$$\mathbf{M}^2 = \begin{pmatrix} M_{2,0,0} & M_{1,1,0} & M_{1,0,1} \\ M_{1,1,0} & M_{0,2,0} & M_{0,1,1} \\ M_{1,0,1} & M_{0,1,1} & M_{0,0,2} \end{pmatrix}, \tag{52}$$

and can be decomposed as $\mathbf{M}^2 = \rho_e \alpha_p^\star (\mathbf{u}_p \otimes \mathbf{u}_p + \boldsymbol{\sigma})$ where $\boldsymbol{\sigma}$ is the non-negative velocity covariance matrix. A full second-order moment closure will solve ten transport equations for the independent moments in eq. (50)–eq. (52) [51]. In this work, we use a reduced second-order moment closure where $\boldsymbol{\sigma}$ is replaced by $\frac{1}{3} tr(\boldsymbol{\sigma})\mathbf{I} = \Theta_p \mathbf{I}$, which corresponds to a Maxwellian distribution. The particle-phase kinetic energy will then be a scalar:

$$M^2 = tr(\mathbf{M}^2) = M_{2,0,0} + M_{0,2,0} + M_{0,0,2} = \rho_e \alpha_p^\star (u_p^2 + 3\Theta_p) \quad \Longrightarrow \quad M^2 = 2\rho_e \alpha_p^\star K_p. \tag{53}$$

[6] The velocity moments can also be defined using a vector/tensor notation. For example, the vector of first-order moments is $\mathbf{M}^1 = \langle \mathbf{u}\rangle$, and the second-order tensor is $\mathbf{M}^2 = \langle \mathbf{u} \otimes \mathbf{u}\rangle$. Higher-order moments are defined similarly using direct products of $\mathbf{u}$. Such notation is particularly useful when working with non-Cartesian coordinates, and when decomposing the velocity into its mean and fluctuating components.

This level of closure corresponds to the Euler equation for the particle phase, and corresponds for example to the case where $f(\mathbf{u})$ is Maxwellian. The central moments, defined by

$$C^l_{i,j,k} = \frac{1}{M^0}\int (u-u_p)^i (v-v_p)^j (w-w_p)^k f(\mathbf{u})\,\mathrm{d}\mathbf{u}, \tag{54}$$

are thus null when l is odd. This fact will be needed to close the spatial flux of M^2, which depends on third-order moments.

3.3. Transport equation for velocity moments

The kinetic model in eq. (23) yields a transport equation for the particle-phase velocity moments. In Cartesian coordinates, we find for $i, j, k \geq 0$ and $l = i + j + k$:[7]

$$\begin{aligned}
\partial_t M^l_{i,j,k} + \partial_x(M^{l+1}_{i+1,j,k} + iP_pM^{l-1}_{i-1,j,k}) + \partial_y(M^{l+1}_{i,j+1,k} + jP_pM^{l-1}_{i,j-1,k}) + \partial_z(M^{l+1}_{i,j,k+1} + kP_pM^{l-1}_{i,j,k-1}) = \\
i\langle u^{i-1}v^jw^kA_{u,x}\rangle + j\langle u^iv^{j-1}w^kA_{u,y}\rangle + k\langle u^iv^jw^{k-1}A_{u,z}\rangle \\
+ i(i-1)\langle u^{i-2}v^jw^kB_{u,xx}\rangle + j(j-1)\langle u^iv^{j-2}w^kB_{u,yy}\rangle + k(k-1)\langle u^iv^jw^{k-2}B_{u,zz}\rangle \\
+ 2ij\langle u^{i-1}v^{j-1}w^kB_{u,xy}\rangle + 2ik\langle u^iv^jw^{k-1}B_{u,xz}\rangle + 2jk\langle u^iv^{j-1}w^{k-1}B_{u,zz}\rangle \\
- \frac{i}{\rho_e}(\partial_x\hat{p}_f + F_{pf,x})M^{l-1}_{i-1,j,k} - \frac{j}{\rho_e}(\partial_y\hat{p}_f + F_{pf,y})M^{l-1}_{i,j-1,k} - \frac{k}{\rho_e}(\partial_z\hat{p}_f + F_{pf,z})M^{l-1}_{i,j,k-1} \\
- i\frac{M^{l-1}_{i-1,j,k}}{\rho_e\alpha^\star_p}(\partial_\mathbf{x}\cdot\mathbf{P}_{pfp})_x - j\frac{M^{l-1}_{i,j-1,k}}{\rho_e\alpha^\star_p}(\partial_\mathbf{x}\cdot\mathbf{P}_{pfp})_y - k\frac{M^{l-1}_{i,j,k-1}}{\rho_e\alpha^\star_p}(\partial_\mathbf{x}\cdot\mathbf{P}_{pfp})_z + C_{i,j,k} + F_{i,j,k} + S_{i,j,k}.
\end{aligned} \tag{55}$$

Here, $C_{i,j,k}$, $F_{i,j,k}$, and $S_{i,j,k}$ are closed given the three moments M^0, $\mathbf{M}^1$ and $\mathbf{M}^2$. Due to conservation of mass and momentum, $C_{0,0,0} = C_{1,0,0} = C_{0,1,0} = C_{0,0,1} = 0$ and $F_{0,0,0} = F_{1,0,0} = F_{0,1,0} = F_{0,0,1} = 0$.

3.3.1. Source terms for velocity moments

The fluid-drag source terms are

$$\begin{aligned}
\langle u^{i-1}v^jw^kA_{u,x}\rangle &= \frac{1}{\tau_p}\left(u_fM^{l-1}_{i-1,j,k} - M^l_{i,j,k}\right) \\
\langle u^iv^{j-1}w^kA_{u,y}\rangle &= \frac{1}{\tau_p}\left(v_fM^{l-1}_{i,j-1,k} - M^l_{i,j,k}\right) \\
\langle u^iv^jw^{k-1}A_{u,z}\rangle &= \frac{1}{\tau_p}\left(w_fM^{l-1}_{i,j,k-1} - M^l_{i,j,k}\right) \\
\langle u^{i-2}v^jw^kB_{u,xx}\rangle &= \frac{1-a}{\tau_p}\left[M^l_{i,j,k} - 2u_pM^{l-1}_{i-1,j,k} + \left(u_p^2 + \frac{2}{3}k_f\right)M^{l-2}_{i-2,j,k}\right] \\
\langle u^iv^{j-2}w^kB_{u,yy}\rangle &= \frac{1-a}{\tau_p}\left[M^l_{i,j,k} - 2v_pM^{l-1}_{i,j-1,k} + \left(v_p^2 + \frac{2}{3}k_f\right)M^{l-2}_{i,j-2,k}\right] \\
\langle u^iv^jw^{k-2}B_{u,zz}\rangle &= \frac{1-a}{\tau_p}\left[M^l_{i,j,k} - 2w_pM^{l-1}_{i,j,k-1} + \left(w_p^2 + \frac{2}{3}k_f\right)M^{l-2}_{i,j,k-2}\right] \\
\langle u^{i-1}v^{j-1}w^kB_{u,xy}\rangle &= \frac{1-a}{\tau_p}\left(M^l_{i,j,k} - u_pM^{l-1}_{i-1,j,k} - v_pM^{l-1}_{i,j-1,k} + u_pv_pM^{l-2}_{i-1,j-1,k}\right) \\
\langle u^{i-1}v^jw^{k-1}B_{u,xz}\rangle &= \frac{1-a}{\tau_p}\left(M^l_{i,j,k} - u_pM^{l-1}_{i-1,j,k} - w_pM^{l-1}_{i,j,k-1} + u_pw_pM^{l-2}_{i-1,j,k-1}\right) \\
\langle u^iv^{j-1}w^{k-1}B_{u,yz}\rangle &= \frac{1-a}{\tau_p}\left(M^l_{i,j,k} - v_pM^{l-1}_{i,j-1,k} - w_pM^{l-1}_{i,j,k-1} + v_pw_pM^{l-2}_{i,j-1,k-1}\right)
\end{aligned} \tag{56}$$

[7] Moments with negative subscripts i, j, k are null.

with fluid velocity components (u_f, v_f, w_f). The inelastic BGK model for collisions introduced in section 3.1.4 yields

$$C_{i,j,k} = \frac{1}{\tau_c}\left(\rho_e \alpha_p^\star G_{i,j,k} - M^l_{i,j,k}\right) \tag{57}$$

where $G_{i,j,k}$ is the moment from f_G. Similarly, the frictional model yields

$$F_{i,j,k} = \frac{1}{\tau_f}\left(\rho_e \alpha_p^\star u_p^i v_p^j w_p^k - M^l_{i,j,k}\right). \tag{58}$$

Finally, the added-mass source term with the coefficients C_ξ and C_u given by (35) is

$$\begin{aligned}
S_{i,j,k} &= C_\xi M^l_{i,j,k} + C_u i\left(u_f M^{l-1}_{i-1,j,k} - M^l_{i,j,k}\right) + C_u j\left(v_f M^{l-1}_{i,j-1,k} - M^l_{i,j,k}\right) + C_u k\left(w_f M^{l-1}_{i,j,k-1} - M^l_{i,j,k}\right) \\
&+ \frac{1}{2}C_u i(i-1)\left[M^l_{i,j,k} - 2u_f M^{l-1}_{i-1,j,k} + \left(u_f^2 + \frac{2}{3}k_f\right)M^{l-2}_{i-2,j,k}\right] + C_u ij\left[M^l_{i,j,k} - u_f M^{l-1}_{i,j-1,k} - v_f M^{l-1}_{i-1,j,k} + u_f v_f M^{l-2}_{i-1,j-1,k}\right] \\
&+ \frac{1}{2}C_u j(j-1)\left[M^l_{i,j,k} - 2v_f M^{l-1}_{i,j-1,k} + \left(v_f^2 + \frac{2}{3}k_f\right)M^{l-2}_{i,j-2,k}\right] + C_u ik\left[M^l_{i,j,k} - u_f M^{l-1}_{i,j,k-1} - w_f M^{l-1}_{i-1,j,k} + u_f w_f M^{l-2}_{i-1,j,k-1}\right] \\
&+ \frac{1}{2}C_u k(k-1)\left[M^l_{i,j,k} - 2w_f M^{l-1}_{i,j,k-1} + \left(w_f^2 + \frac{2}{3}k_f\right)M^{l-2}_{i,j,k-2}\right] + C_u jk\left[M^l_{i,j,k} - v_f M^{l-1}_{i,j,k-1} - w_f M^{l-1}_{i,j-1,k} + v_f w_f M^{l-2}_{i,j-1,k-1}\right].
\end{aligned} \tag{59}$$

For the two-fluid model using in this work, we will need source terms for seven moments up to second order, i.e., for $(i, j, k) \in \{(0,0,0), (1,0,0), (0,1,0), (0,0,1), (2,0,0), (0,2,0), (0,0,2)\}$.

3.3.2. Free-transport flux of velocity moments

The only unclosed term in eq. (55) is the free-transport spatial flux M^3, which is closed using HyQMOM [18, 19]. In the absence of P_p (i.e., very dilute flow), HyQMOM ensures that the system of moment equations is hyperbolic. In general, if we keep moments up to M^2, HyQMOM requires that the central moments $C^3 = 0$, which corresponds to the anisotropic Gaussian closure [51]. In particular,

$$\begin{aligned}
M^3_{3,0,0} &= M^0(3u_p C^2_{2,0,0} + u_p^3) = \rho_e \alpha_p^\star (3\Theta_p + u_p^2)u_p \\
M^3_{2,1,0} &= M^0(v_p C^2_{2,0,0} + 2u_p C^2_{1,1,0} + u_p^2 v_p) = \rho_e \alpha_p^\star (\Theta_p + u_p^2)v_p \\
M^3_{2,0,1} &= M^0(w_p C^2_{2,0,0} + 2u_p C^2_{1,0,1} + u_p^2 w_p) = \rho_e \alpha_p^\star (\Theta_p + u_p^2)w_p \\
M^3_{1,1,1} &= M^0(u_p C^2_{0,1,1} + v_p C^2_{1,0,1} + w_p C^2_{1,1,0} + u_p v_p w_p) = \rho_e \alpha_p^\star u_p v_p w_p
\end{aligned} \tag{60}$$

and the other third-order moments are found by permuting the indices. In these closures, the second-order central moments are treated as isotropic:

$$C^2_{i,j,k} = \Theta_p(\delta_{i,2} + \delta_{j,2} + \delta_{k,2}) \quad \Longrightarrow \quad \mathbf{C}^2 = \Theta_p \mathbf{I}. \tag{61}$$

The components of the spatial flux for M^2 are then

$$\begin{aligned}
F^2_x &= M^3_{3,0,0} + M^3_{1,2,0} + M^3_{1,0,2} = \rho_e \alpha_p^\star (5\Theta_p + u_p^2 + v_p^2 + w_p^2)u_p \\
F^2_y &= M^3_{2,1,0} + M^3_{0,3,0} + M^3_{0,1,2} = \rho_e \alpha_p^\star (5\Theta_p + u_p^2 + v_p^2 + w_p^2)v_p \\
F^2_z &= M^3_{2,0,1} + M^3_{0,2,1} + M^3_{0,0,3} = \rho_e \alpha_p^\star (5\Theta_p + u_p^2 + v_p^2 + w_p^2)w_p
\end{aligned} \tag{62}$$

i.e., the flux vector is $\mathbf{F}^2 = 2\rho_e \alpha_p^\star (K_p + \Theta_p)\mathbf{u}_p = M^2 \mathbf{u}_p + 2\rho_e \alpha_p^\star \Theta_p \mathbf{u}_p$. Using, for example, extended kinetic theory [3], the momentum flux could be extended to viscous granular flows by adding the appropriate closures. For the high-speed flows considered in this work, such terms are very small compared to the granular pressure terms.

3.3.3. Velocity moment equations in two-fluid model

In this work, we consider velocity moments up to second order. Thus, we must solve five transport equations, four equations for mass and momentum,

$$\partial_t M^0_{0,0,0} + \partial_x M^1_{1,0,0} + \partial_y M^1_{0,1,0} + \partial_z M^1_{0,0,1} = S_a \tag{63}$$

$$\begin{aligned}
\partial_t M^1_{1,0,0} + \partial_x (M^2_{2,0,0} + P_p M^0_{0,0,0}) + \partial_y M^2_{1,1,0} + \partial_z M^2_{1,0,1} &= \langle A_{u,x} \rangle - \alpha^\star_p (\partial_x \hat{p}_f + F_{pf,x}) - (\partial_{\mathbf{x}} \cdot \mathbf{P}_{pfp})_x + (\mathbf{S}_{gp})_x \\
\partial_t M^1_{0,1,0} + \partial_x M^2_{1,1,0} + \partial_y (M^2_{0,2,0} + P_p M^0_{0,0,0}) + \partial_z M^2_{0,1,1} &= \langle A_{u,y} \rangle - \alpha^\star_p (\partial_y \hat{p}_f + F_{pf,y}) - (\partial_{\mathbf{x}} \cdot \mathbf{P}_{pfp})_y + (\mathbf{S}_{gp})_y \\
\partial_t M^1_{0,0,1} + \partial_x M^2_{1,0,1} + \partial_y M^2_{0,1,1} + \partial_z (M^2_{0,0,2} + P_p M^0_{0,0,0}) &= \langle A_{u,z} \rangle - \alpha^\star_p (\partial_z \hat{p}_f + F_{pf,z}) - (\partial_{\mathbf{x}} \cdot \mathbf{P}_{pfp})_z + (\mathbf{S}_{gp})_z
\end{aligned} \tag{64}$$

and the sum of the three equations for $M_{2,0,0}$, $M_{0,2,0}$ and $M_{0,0,2}$ (using tensor notation):

$$\partial_t M^2 + \partial_{\mathbf{x}} \cdot (M^2 + 2\rho_e \alpha^\star_p \Theta_p + 2\rho_e \alpha^\star_p P_p)\mathbf{u}_p = -2D_E - 2\alpha^\star_p \mathbf{u}_p \cdot (\partial_{\mathbf{x}} \hat{p}_f + \mathbf{F}_{pf}) - 2\mathbf{u}_p \cdot (\partial_{\mathbf{x}} \cdot \mathbf{P}_{pfp}) - 2H_p + 2S_K. \tag{65}$$

The free-transport pressure tensor in eq. (64) is

$$\begin{bmatrix} M^2_{2,0,0} & M^2_{1,1,0} & M^2_{1,0,1} \\ M^2_{1,1,0} & M^2_{0,2,0} & M^2_{0,1,1} \\ M^2_{1,0,1} & M^2_{0,1,1} & M^2_{0,0,2} \end{bmatrix} = M^0_{0,0,0}(\mathbf{u}_p \otimes \mathbf{u}_p + \Theta_p \mathbf{I}), \tag{66}$$

whose trace is $M^2 = M_{2,0,0} + M_{0,2,0} + M_{0,0,2} = 2M^0_{0,0,0} K_p$. In eq. (65), H_p is particle-phase kinetic-to-internal-energy transfer due to inelastic collisions and friction. In the fluid-phase total energy balance, the fluid-drag contribution is

$$D_E = \frac{1}{\tau_p}[M^2 - \rho_e \alpha^\star_p \mathbf{u}_f \cdot \mathbf{u}_p - (1-a)(\langle B_{u,xx} \rangle + \langle B_{u,yy} \rangle + \langle B_{u,zz} \rangle)] = \frac{\rho_e \alpha^\star_p}{\tau_p}[3a\Theta_p - 2(1-a)k_f + \mathbf{u}_{pf} \cdot \mathbf{u}_p]. \tag{67}$$

Thus, D_E represents kinetic-energy transfer to the fluid from particles ($D_E > 0$) or vice versa ($D_E < 0$).

3.4. Final form of the nine-equation, two-fluid model

The mass balance in eq. (63) can be rewritten in a more familiar form using tensor notation:

$$\partial_t \rho_e \alpha^\star_p + \partial_{\mathbf{x}} \cdot \rho_e \alpha^\star_p \mathbf{u}_p = S_a. \tag{68}$$

Likewise, the momentum balance in eq. (64) can be rewritten as

$$\partial_t \rho_e \alpha^\star_p \mathbf{u}_p + \partial_{\mathbf{x}} \cdot \rho_e \alpha^\star_p (\mathbf{u}_p \otimes \mathbf{u}_p + \Theta_p \mathbf{I} + P_p \mathbf{I}) = -\frac{\rho_e \alpha^\star_p}{\tau_p} \mathbf{u}_{pf} - \alpha^\star_p (\partial_{\mathbf{x}} \hat{p}_f + \mathbf{F}_{pf}) - \partial_{\mathbf{x}} \cdot \mathbf{P}_{pfp} + \mathbf{S}_{gp}. \tag{69}$$

Conservation of momentum requires that the drag contribution in the fluid phase be defined by

$$\mathbf{D} = \frac{\rho_e \alpha^\star_p}{\tau_p} \mathbf{u}_{pf} \tag{70}$$

in eq. (8). The kinetic-energy balance in eq. (65) can be rewritten as

$$\partial_t \rho_e \alpha^\star_p K_p + \partial_{\mathbf{x}} \cdot [\rho_e \alpha^\star_p (K_p + \Theta_p + P_p)\mathbf{u}_p] = -D_E - \alpha^\star_p \mathbf{u}_p \cdot (\partial_{\mathbf{x}} \hat{p}_f + \mathbf{F}_{pf}) - \mathbf{u}_p \cdot (\partial_{\mathbf{x}} \cdot \mathbf{P}_{pfp}) + S_K - H_p. \tag{71}$$

The balance for the total energy E_p can be found by summing eq. (47) and eq. (71). Comparing the total-energy balance with eq. (9) (see table 1), it can be easily shown that the total energy of the two phases is conserved.

To conclude the definition of the two-fluid model, note that given α_p and the two conserved variables for the phase masses, α_a is found from

$$\alpha_a = \frac{\kappa}{1+\kappa}\alpha_f \qquad \text{for} \qquad \kappa = \frac{\rho_e \alpha^\star_p - \rho_p \alpha_p}{\rho_f \alpha^\star_f} = \frac{\alpha_a}{\alpha^\star_f} \tag{72}$$

Table 1: Nine-equation, two-fluid model for monodisperse fluid–particle flow with added mass, internal energy, and PTKE. Gravity $\mathbf{g}$ is included in the model for completeness. The $\mathbf{P}_{pfp}$ term is written here as a force in the momentum balances, but could also be written as a particle-phase pressure flux. In either case, $\mathbf{P}_{pfp}$ does not act as a source term for Θ_p.

Mass balances:

$$\partial_t \rho_f \alpha_f^\star + \partial_\mathbf{x} \cdot \rho_f \alpha_f^\star \mathbf{u}_f = -S_a$$
$$\partial_t \rho_e \alpha_p^\star + \partial_\mathbf{x} \cdot \rho_e \alpha_p^\star \mathbf{u}_p = S_a$$
$$\partial_t \rho_p \alpha_p + \partial_\mathbf{x} \cdot \rho_p \alpha_p \mathbf{u}_p = 0$$

Momentum balances:

$$\partial_t \rho_f \alpha_f^\star \mathbf{u}_f + \partial_\mathbf{x} \cdot (\rho_f \alpha_f^\star \mathbf{u}_f \otimes \mathbf{u}_f + \hat{p}_f \mathbf{I} + \mathbf{P}_{pfp}) = \frac{\rho_e \alpha_p^\star}{\tau_p} \mathbf{u}_{pf} + \alpha_p^\star (\partial_\mathbf{x} \hat{p}_f + \mathbf{F}_{pf}) + \partial_\mathbf{x} \cdot \mathbf{P}_{pfp} - \mathbf{S}_{fp} + \rho_f \alpha_f^\star \mathbf{g}$$

$$\partial_t \rho_e \alpha_p^\star \mathbf{u}_p + \partial_\mathbf{x} \cdot \rho_e \alpha_p^\star (\mathbf{u}_p \otimes \mathbf{u}_p + \Theta_p \mathbf{I} + P_p \mathbf{I}) = -\frac{\rho_e \alpha_p^\star}{\tau_p} \mathbf{u}_{pf} - \alpha_p^\star (\partial_\mathbf{x} \hat{p}_f + \mathbf{F}_{pf}) - \partial_\mathbf{x} \cdot \mathbf{P}_{pfp} + \mathbf{S}_{fp} + \rho_e \alpha_p^\star \mathbf{g}$$

Fluid-phase energy balances (total + PTKE):

$$\partial_t \rho_f \alpha_f^\star E_f + \partial_\mathbf{x} \cdot (\rho_f \alpha_f^\star \mathbf{u}_f E_f + \alpha_f^\star \mathbf{u}_f \hat{p}_f + \alpha_p^\star \mathbf{u}_p \hat{p}_f + \mathbf{u}_p \cdot \mathbf{P}_{pfp}) =$$
$$\frac{\rho_e \alpha_p^\star}{\tau_p} [3a\Theta_p - 2(1-a)k_f + \mathbf{u}_{pf} \cdot \mathbf{u}_p] + \alpha_p^\star \mathbf{u}_p \cdot (\partial_\mathbf{x} \hat{p}_f + \mathbf{F}_{pf}) + \mathbf{u}_p \cdot (\partial_\mathbf{x} \cdot \mathbf{P}_{pfp}) + H_{pf} - S_E + \rho_f \alpha_f^\star \mathbf{u}_f \cdot \mathbf{g}$$

$$\partial_t \rho_f \alpha_f^\star k_f + \partial_\mathbf{x} \cdot \rho_f \alpha_f^\star \mathbf{u}_f k_f = -\frac{2}{3} \rho_f \alpha_f^\star k_f \partial_\mathbf{x} \cdot \mathbf{u}_f + \frac{\rho_e \alpha_p^\star}{\tau_p} [3a\Theta_p - 2(1-a)k_f + u_{pf}^2 - C_f k_f]$$

Particle-phase energy balances (kinetic + internal):

$$\partial_t \rho_e \alpha_p^\star K_p + \partial_\mathbf{x} \cdot \rho_e \alpha_p^\star (K_p + \Theta_p + P_p) \mathbf{u}_p =$$
$$-\frac{\rho_e \alpha_p^\star}{\tau_p} [3a\Theta_p - 2(1-a)k_f + \mathbf{u}_{pf} \cdot \mathbf{u}_p] - \alpha_p^\star \mathbf{u}_p \cdot (\partial_\mathbf{x} \hat{p}_f + \mathbf{F}_{pf}) - \mathbf{u}_p \cdot (\partial_\mathbf{x} \cdot \mathbf{P}_{pfp}) + S_K - H_p + \rho_e \alpha_p^\star \mathbf{u}_p \cdot \mathbf{g}$$

$$\partial_t \rho_e \alpha_p^\star e_p + \partial_\mathbf{x} \cdot \rho_e \alpha_p^\star e_p \mathbf{u}_p = -H_{pf} + S_e + H_p$$

with $\alpha_f = 1 - \alpha_p$, and then $\alpha_p^\star = \alpha_p + \alpha_a$ and $\alpha_f^\star = \alpha_f - \alpha_a$. Thus, for constant ρ_p, the primitive variables (α_p, ρ_e, ρ_f, $\mathbf{u}_p$, $\mathbf{u}_f$, K_p, e_p, E_f, k_f) are uniquely defined from the conserved variables ($\rho_p \alpha_p$, $\rho_e \alpha_p^\star$, $\rho_f \alpha_f^\star$, $\rho_e \alpha_p^\star \mathbf{u}_p$, $\rho_f \alpha_f^\star \mathbf{u}_f$, $\rho_e \alpha_p^\star K_p$, $\rho_e \alpha_p^\star e_p$, $\rho_f \alpha_f^\star E_f$, $\rho_f \alpha_f^\star k_f$). The nine-equation, two-fluid model for fluid–particle flow with added mass, internal energy, and PTKE is summarized in table 1 with parameters defined in table 2. Example values for the model constants in gas–particle flows are given in table 3. However, for specific fluid and solid phases, the thermodynamic properties must be specified for each application. For example, it may be necessary to account for the temperature dependence of the heat capacities when defining the internal energies, and the fluid-phase viscosity. For the shock–particle cases, the definition of the drag coefficient C_D may need to a depend on the Mach number [5].

4. Numerical implementation

In this work, the coupled fluid–particle moment equations are implemented in a 1-D hyperbolic equation solver. Given that the overall system of equations is hyperbolic, the extension to three dimensions on a structured Cartesian grid would use the same approach with directional splitting [27]. To increase robustness and stability, we employ operator splitting for the spatial fluxes and source terms.

Table 2: Parameters appearing in two-fluid model for monodisperse fluid–particle flow in table 1. In the definition of $\mathbf{R}$, the parameters must satisfy $3B_1 + B_2 > 0$ so that $tr(\mathbf{R}) = u_{pf}^2$ and $C_{pfp} > 0$. The correlations for B_1 and B_2 come from [53], and are valid for a limited range of Re_p and $\alpha_p > 0.01$. For smaller α_p, B_1 can be taken as constant. The thermodynamic temperatures T_f and T_p are found from the internal energies of their respective phases. λ_f is the fluid-phase thermal conductivity.

$$\kappa = \frac{\rho_e \alpha_p^\star - \rho_p \alpha_p}{\rho_f \alpha_f^\star} \qquad \alpha_f = 1 - \alpha_p \qquad \alpha_a = \frac{\kappa}{1+\kappa}\alpha_f \qquad \alpha_p^\star = \alpha_p + \alpha_a \qquad \alpha_f^\star = \alpha_f - \alpha_a \qquad \mathbf{u}_{pf} = \mathbf{u}_p - \mathbf{u}_f$$

$$\mathbf{R} = \frac{B_1 u_{pf}^2 \mathbf{I} + B_2 \mathbf{u}_{pf} \otimes \mathbf{u}_{pf}}{3B_1 + B_2} \quad \mathbf{P}_{pfp} = C_{pfp}\rho_f \alpha_p^\star \mathbf{R} \quad \mathbf{F}_{pf} = \mathbf{R}\cdot\partial_{\mathbf{x}}\rho_f - (\gamma_f - 1)\rho_f(\partial_{\mathbf{x}}\cdot\mathbf{u}_f)\mathbf{u}_{pf} + C_l \rho_f \mathbf{u}_{pf} \times (\partial_{\mathbf{x}} \times \mathbf{u}_f)$$

$$S_a = \frac{\rho_f}{\tau_a}(c_m^\star \alpha_f \alpha_p - \alpha_a) \qquad \mathbf{S}_{fp} = \max(S_a, 0)\,\mathbf{u}_f + \min(S_a, 0)\,\mathbf{u}_p \qquad S_E = \max(S_a, 0)\,E_f + \min(S_a, 0)\,E_p$$

$$S_K = \max(S_a, 0)\,K_f + \min(S_a, 0)\,K_p \qquad S_e = \max(S_a, 0)\,e_f + \min(S_a, 0)\,e_p \qquad H_{pf} = \frac{6\alpha_p^\star \lambda_f Nu}{d_p^2}(T_p - T_f)$$

$$Re_p = \frac{d_p u_{pf}}{\nu_f} \quad Pr_f = \frac{\rho_f C_{p,f} \nu_f}{\lambda_f} \quad Nu = (7 - 10\alpha_f + 5\alpha_f^2)(1 + 0.7 Re_p^{0.2} Pr_f^{1/3}) + (1.33 - 2.4\alpha_f + 1.2\alpha_f^2) Re_p^{0.7} Pr_f^{1/3}$$

$$c_m^\star = \frac{1}{2}\min(1 + 2\alpha_p, 2) \qquad \tau_a = C_a \tau_p \qquad \tau_p = \frac{4\rho_e d_p^2}{3\mu_f C_D Re_p} \qquad C_D = \frac{24}{Re_p}\left(1 + 0.15 Re_p^{0.687}\right)\alpha_f^{-2.65}$$

$$\tau_c = \frac{d_p\sqrt{\pi}}{12\alpha_p g_0 \Theta_p^{1/2}} \qquad \tau_f = \frac{2c_f}{\max(|\partial_{\mathbf{x}}\cdot\mathbf{u}_p|, 1/\tau_c)}\left[1 + \tanh\left(\frac{\alpha_p - \alpha_{max}}{\Delta_f}\right)\right]^{-1} \qquad g_0 = \frac{1 + \alpha_f}{2\alpha_f^3}$$

$$p_f = (\gamma_f - 1)\rho_f e_f - \gamma_f p_{\infty,f} \qquad e_f = E_f - \frac{1}{2}u_f^2 - k_f \qquad \Theta_p = \frac{2}{3}K_p - \frac{1}{3}u_p^2 \qquad H_p = \rho_e \alpha_p^\star \left[\frac{1}{\tau_c}(1 - e_c^2) + \frac{1}{\tau_f}\right]\Theta_p$$

$$\hat{p}_f = p_f + \frac{2}{3}\rho_f k_f \qquad P_p = P_c + P_f \qquad P_c = 2(1 + e_c)\alpha_p g_0 \Theta_p \qquad P_f = \frac{p_f \alpha_p g_0}{2\rho_e \alpha_p^\star}\left[1 + \tanh\left(\frac{\alpha_p - \alpha_{max}}{\Delta_f}\right)\right]$$

$$T_f = \frac{\gamma_f e_f}{C_{p,f}} \qquad T_p = \frac{e_p}{C_{V,p}} \qquad C_f^{-1} = \alpha_p[1 + 1.25\alpha_f^3 \exp(-\alpha_p \alpha_f^{1/2} Re_p^{1/2})] \qquad a = \frac{\rho_p + \rho_f a_{min}}{\rho_p + \rho_f} \qquad C_{pfp} = c_m^\star$$

Table 3: Example model constants for gas–particle flows.

$$B_1 = \max(1.0915 - 0.95 Re_p^{0.02} + 0.01 \ln \alpha_p, -B_2) \quad B_2 = -\max(0.4046 Re_p^{-0.3} - 0.042, 0)$$

$$e_c = 0.9 \quad a_{min} = 0.5 \quad C_l = 0.5 \quad C_a = 1 \quad c_f = 0.01 \quad \alpha_{max} = 0.63 \quad \Delta_f = 0.01 \quad p_f = 533,333 \text{ kg/m/s}^2$$

$$\nu_f = 1.36 \times 10^{-5} \text{ m}^2/\text{s} \quad \gamma_f = 1.4 \quad \lambda_f = 0.03 \text{ kg m/s}^3/\text{K} \quad C_{p,f} = 1300 \text{ m}^2/\text{s}^2/\text{K} \quad C_{V,p} = 900 \text{ m}^2/\text{s}^2/\text{K}$$

4.1. Overall solution algorithm

Fluid and added-mass phases. The following terms have been implemented for the fluid phase when solving the 1-D versions of eq. (7)–eq. (10):

1. The *pfp* pressure P_{pfp} in the spatial flux.
2. The buoyancy, unsteady drag F_{pf}, and *pfp* pressure coupled to the particle phase.
3. The drag terms, including PTKE, coupled to the particle phase.
4. The convective heat-transfer term coupled to the particle phase.
5. The added-mass source terms coupled to the particle phase.

Particle phase. The following items have been implemented for the particle phase when solving the 1-D versions of eq. (68)–eq. (71):

1. HyQMOM to compute the free-transport closures with realizability checking.
2. The collisional and frictional particle pressures.
3. The buoyancy, unsteady drag, and *pfp* pressure coupled to the fluid phase (see section 4.2.4).
4. The collision source terms, including internal energy.
5. The friction source terms, including internal energy.
6. The drag terms, including PTKE, coupled to the fluid phase.
7. The convective heat-transfer term.
8. The added-mass source terms (see section 4.4).

A operator-splitting approach is employed to solve the coupled moment equations (i.e., for fluid and particles) separately for each item listed above. The splitting errors are reduced by using a Strang operator splitting as in [27] such that

$$\mathbf{Y}^n \xrightarrow{\mathcal{H}^{\frac{\Delta t}{2}}} \mathbf{Y}^{n+\frac{1}{4}} \xrightarrow{\mathcal{S}^{\Delta t}} \mathbf{Y}^{n+\frac{3}{4}} \xrightarrow{\mathcal{H}^{\frac{\Delta t}{2}}} \mathbf{Y}^{n+1} \tag{73}$$

with $\mathbf{Y}^n$ the vector of conserved variables at time t^n, $\mathbf{Y}^{n+1}$ the vector of conserved variables at time t^{n+1}, $\mathcal{H}^{\frac{\Delta t}{2}}$ the hyperbolic step for half a time step and $\mathcal{S}^{\Delta t}$ the integration of all source terms for a time step.

In the first step, the hyperbolic part of the system is solved including spatial fluxes and buoyancy-like terms. The spatial fluxes are approximated by an AUSM$^+$up scheme [34] for the particle phase and a HLLC scheme [50] for the fluid phase in the same fashion as in [27]. The eigenvalues for the spatial flux are found numerically using a subroutine for the Jacobian matrix that was generated symbolically. The first four eigenvalues are used to compute the particle speed of sound required for the AUSM$^+$up scheme, while the three other eigenvalues are used to define the left and right wave speeds in HLLC. The overall time step is based on the maximum particle and fluid eigenvalue. To complete the hyperbolic step, the changes due to buoyancy-like terms are computed using the HLLC reconstructions of primitive variables. Next, the changes in the moments due to the collisional and frictional source terms are computed. Finally, the changes in the moments due to drag and heat transfer are computed. The collisions, friction, drag, and heat transfer are handled with semi-analytical solutions.

When the velocity variance is extremely small (or negative due to round-off error), application of HyQMOM to find M_3 is ill-conditioned. Thus, realizability is checked after each sub-step and the velocity moments are corrected if needed. Based on numerical experiments, corrections are rarely applied and when they are it usually occurs at the interface with 'particle-free' regions. In the simulations, to avoid division by zero, such regions are initialized with a tiny particle number density. Thus, applying the realizability corrections has no impact on the observable quantities. The Jacobian matrix needed for the hyperbolic solver is computed symbolically from eq. (74), and only the magnitudes of the largest and smallest eigenvalues are required to define the HLL fluxes. In general, unless the particle phase is very dense so that P_f is significant, the largest/smallest eigenvalues correspond to the fluid phase, albeit modified by the presence of the particles.

4.2. Numerical treatment of the hyperbolic step

The hyperbolic step encompasses the 1-D spatial fluxes and the buoyancy-like terms leading to the following system:

$$\begin{aligned}
\partial_t \rho_p \alpha_p &= -\partial_x \rho_p \alpha_p u_p, \\
\partial_t \rho_e \alpha_p^\star &= -\partial_x \rho_e \alpha_p^\star u_p, \\
\partial_t \rho_e \alpha_p^\star u_p &= -\partial_x \rho_e \alpha_p^\star (u_p^2 + \Theta_p + P_p) - B, \\
\partial_t \rho_e \alpha_p^\star K_p &= -\partial_x \rho_e \alpha_p^\star (K_p + \Theta_p + P_p) u_p - B u_p, \\
\partial_t \rho_e \alpha_p^\star e_p &= -\partial_x \rho_e \alpha_p^\star e_p u_p,
\end{aligned} \tag{74}$$

$$\begin{aligned}
\partial_t \rho_f \alpha_f^\star &= -\partial_x \rho_f \alpha_f^\star u_f, \\
\partial_t \rho_f \alpha_f^\star u_f &= -\partial_x (\rho_f \alpha_f^\star u_f^2 + \hat{p}_f + P_{pfp}) + B, \\
\partial_t \rho_f \alpha_f^\star E_f &= -\partial_x \cdot (\rho_f \alpha_f^\star u_f E_f + \alpha_f^\star u_f \hat{p}_f + \alpha_p^\star u_p \hat{p}_f + P_{pfp} u_p) + B u_p, \\
\partial_t \rho_f \alpha_f^\star k_f &= -\partial_x \rho_f \alpha_f^\star u_f k_f - \frac{2}{3} \rho_f \alpha_f^\star k_f \partial_x u_f,
\end{aligned}$$

where $P_{pfp} = C_{pfp} \rho_f \alpha_p^\star u_{pf}^2$, $F_{pf} = u_{pf}^2 \partial_x \rho_f - (\gamma_f - 1) \rho_f u_{pf} \partial_x u_f$ with $u_{pf} = u_p - u_f$, and the 1-D buoyancy-like term:

$$B = \alpha_p^\star (\partial_x \hat{p}_f + F_{pf}) + \partial_x P_{pfp} \tag{75}$$

are computed from reconstructed quantities. These terms are also included in this step to keep a discrete consistency between the pressure gradients.

The computation of spatial fluxes can be tedious because of the discontinuous nature of shocks in the fluid phase and particle moments for particle fronts. One approach is to employ a classic HLL scheme for the full system of equations with first-order reconstructions of quantities [20]. This approach is very robust, but introduces excessive diffusion of discontinuities, which can be prohibitive for the accurate simulation of strong shocks or thin particle layers. An improvement can be obtained by considering higher-order reconstructions to better capture discontinuities. In [51], a MUSCL reconstruction with a second-order Runge–Kutta integration in time is applied to a moment method leading to a clear reduction of numerical diffusion. However, this improvement does not cure the severe diffusion of the particle front in our case because of the large disparity in magnitude of the fluid and particle eigenvalues. As explained above, the particle eigenvalues are usually smaller by several orders of magnitude unless the volume fraction approaches the packing limit. Indeed, the HLL scheme relying on minimum and maximum eigenvalues of the full system overestimates the particle propagation waves, leading to undesirable numerical diffusion of the particle-phase quantities.

This observation is the main motivation of splitting the system into particle and fluid parts treated with different flux reconstructions. In this work, the approach proposed in [27] is applied to the system of equations in eq. (74). It consists of a combination of AUSM$^+$up scheme [34] for the particle phase, and an HLLC scheme [50] for the fluid phase. As for the HLL scheme used in [20], the numerical fluxes using upwind reconstruction are first order in space and time, but with enhanced particle front capturing due to the AUSM$^+$up scheme and contact discontinuity capturing in the fluid thanks to the HLLC scheme. A higher-order extension of the fluid part is also proposed by using higher-order reconstructions and a multistage integration in time based on Runge–Kutta schemes [23].

4.2.1. AUSM$^+$up scheme for particle phase

The 1-D equation system for the particle phase, supplemented with the continuity equation of the pure particle phase, is written as

$$\begin{aligned}
\partial_t \rho_p \alpha_p &= -\partial_x \rho_p \alpha_p u_p, \\
\partial_t \rho_e \alpha_p^\star &= -\partial_x \rho_e \alpha_p^\star u_p, \\
\partial_t \rho_e \alpha_p^\star u_p &= -\partial_x \rho_e \alpha_p^\star (u_p^2 + \Theta_p + P_p), \\
\partial_t \rho_e \alpha_p^\star K_p &= -\partial_x \rho_e \alpha_p^\star (K_p + \Theta_p + P_p) u_p, \\
\partial_t \rho_e \alpha_p^\star e_p &= -\partial_x \rho_e \alpha_p^\star e_p u_p.
\end{aligned} \tag{76}$$

The particle phase has its own equation of state where compressibility is a result of volume-fraction variations:

$$p_p = \rho_e \alpha_p^\star (\Theta_p + P_p) = EOS(\rho_e \alpha_p^\star, \alpha_p, \Theta_p). \tag{77}$$

The compaction wave speed a_p (analogous to the fluid speed of sound) can be computed from the pressure derivatives [45]:

$$a_p = \frac{1}{\rho_p} \sqrt{\rho_p \left.\frac{\partial p_p}{\partial \alpha_p}\right|_{\Theta_p} + \frac{2}{3} \frac{\Theta_p}{\alpha_p^2} \left.\frac{\partial p_p}{\partial \Theta_p}\right|_{\alpha_p}^2}. \tag{78}$$

However, eq. (78) was developed for standard particle systems where pressure is defined such that $p_p = EOS(\alpha_p, \Theta_p)$ with constant ρ_p.

In our model, p_p also depends on fluid moments, and a_p is computed from the eigenvalues of the reduced system eq. (76) to account for added mass. The eigenvalues are not necessarily symmetric and the speed of sound is computed using the minimum and maximum values as

$$a_p = \max(u_p - \lambda_{p,min}, \lambda_{p,max} - u_p). \tag{79}$$

In gas–particle systems where $\rho_e \approx \rho_p$, computing a_p from eq. (78) or eq. (79) is almost equivalent. However, ρ_e can become several orders of magnitude higher than ρ_p in bubbly flows and a_p needs to be computed from the eigenvalues of the system to avoid stability issues.

The main difficulty when dealing with eq. (76) is the granular pressure p_p, which can take values from zero (low volume fraction) to extremely large (close to packing limit when P_f prevails). In other words, the Riemann solver needs to deal with a pressure-less system and a low-Mach limit, which are both known to cause problems with standard Godunov-type solvers [24]. AUSM-family schemes [35] are perfect candidates to handle the pressure-less limit as they split the flux into convective and pressure parts, and have the capability to solve near-vacuum flows [33]. Moreover, extra diffusion terms are introduced in the AUSM$^+$up scheme to handle the low-Mach limit [34].

The AUSM$^+$up scheme applied to the particle system from eq. (76) leads to the particle flux vector:

$$\mathbf{f}_p = \dot{m}_p \mathbf{\Psi}_p + \mathbf{\Pi}_p \tag{80}$$

with the mass flux $\dot{m}_p = \rho_e \alpha_p^\star u_p$, the quantity vector $\mathbf{\Psi}_p = (\alpha_p \rho_p / \alpha_p^\star \rho_e, 1, u_p, K_p, e_p)$ and the pressure flux $\mathbf{\Pi}_p = (0, 0, p_p, p_p u_p, 0)$. In the original AUSM scheme [34], the pressure flux is only non-zero for momentum, while enthalpy was transported for energy. In [27], the pseudo-thermal energy Θ_p is solved, and the pressure term is not included in the flux. Here, the kinetic energy K_p is solved and requires to consider a pressure flux consistent with the momentum. To do so, the quantity vector is simply upwinded:

$$\mathbf{\Psi}_p = \begin{cases} \mathbf{\Psi}_p^L, & \text{if } \dot{m}_p \leqslant 0; \\ \mathbf{\Psi}_p^R, & \text{otherwise,} \end{cases} \tag{81}$$

with $\mathbf{\Psi}_p^L$ and $\mathbf{\Psi}_p^R$ the left and right reconstructions of $\mathbf{\Psi}_p$ at a given face.

Then the mass flux is computed from the face Mach number $\mathcal{M}_p^{1/2}$ as

$$\dot{m}_p = a_p^{1/2}\mathcal{M}_p^{1/2}\begin{cases}\rho_e^L\alpha_p^{\star,L}, & \text{if } \mathcal{M}_p^{1/2} \leqslant 0;\\ \rho_e^R\alpha_p^{\star,R}, & \text{otherwise.}\end{cases} \tag{82}$$

The face compaction wave speed $a_p^{1/2}$ is computed as in [27] from the following mass average:

$$a_p^{1/2} = \sqrt{\frac{\rho_e^L\alpha_p^{\star,L}(a_p^L)^2 + \rho_e^R\alpha_p^{\star,R}(a_p^R)^2}{\rho_e^L\alpha_p^{\star,L} + \rho_e^R\alpha_p^{\star,R}}} + \epsilon \tag{83}$$

with $\epsilon = 1 \times 10^{-10}$ a small number to avoid division by zero when the compaction wave speed is null. In the same manner, the face density is defined as

$$\rho_e^{1/2} = \frac{\rho_e^L\alpha_p^{\star,L} + \rho_e^R\alpha_p^{\star,R}}{2}, \tag{84}$$

and the left, right, and averaged Mach numbers are computed from $a_p^{1/2}$:

$$\mathcal{M}_p^L = \frac{u_p^L}{a_p^{1/2}}, \qquad \mathcal{M}_p^R = \frac{u_p^R}{a_p^{1/2}}, \qquad \bar{\mathcal{M}}_p^2 = \frac{(u_p^L)^2 + (u_p^R)^2}{2(a_p^{1/2})^2}. \tag{85}$$

Finally, the face Mach number $\mathcal{M}_p^{1/2}$ related to the convective flux and the face pressure $\mathcal{P}_p^{1/2}$ related to the pressure flux are computed from the split Mach number and pressure polynomials $\mathscr{M}_4^{\pm}$ and $\mathscr{P}_5^{\pm}$ [33] as

$$\mathcal{M}_p^{1/2} = \mathscr{M}_4^+(\mathcal{M}_p^L) + \mathscr{M}_4^-(\mathcal{M}_p^R) - \frac{k_p}{f_a}\max(1 - \sigma\bar{\mathcal{M}}_p^2, 0)\frac{p_p^R - p_p^L}{(\rho_e^{1/2} + \epsilon)(a_p^{1/2})^2}, \tag{86}$$

$$p_p^{1/2} = \mathscr{P}_5^+(\mathcal{M}_p^L)p_p^L + \mathscr{P}_5^-(\mathcal{M}_p^R)p_p^R - 2k_u f_a \mathscr{P}_5^+(\mathcal{M}_p^L)\mathscr{P}_5^-(\mathcal{M}_p^R)\rho_e^{1/2}(a_p^{1/2} - \epsilon)(u_p^R - u_p^L) \tag{87}$$

with $k_p = 0.25$, $k_u = 0.75$, $f_a = 1$, and $\sigma = 1$ parameters controlling the pressure and velocity diffusion terms. The pressure flux for energy is then computed as $a_p^{1/2}\mathcal{M}_p^{1/2}p_p^{1/2}$.

In [27], left and right reconstructions were computed with a WENO5 scheme. However, the low dissipation properties of such reconstructions require a slope limiter and an additional diffusion term in the mass flux to remain stable near strong particle discontinuities or close to the packing limit. It has been found in this work that adding diffusion in the mass flux leads to the loss of realizability of the scheme. This could be due to the tight coupling of fluid and particle phases through the added-mass part. Then, a small diffusion in the particle part can lead to some inconsistency of the fluid quantities. Hence, first-order upwind reconstructions are used in the following numerical examples. Note that this choice does not imply the loss of the inherent capturing of the particle front of AUSM$^+$up as it will be demonstrated below.

4.2.2. HLLC scheme for fluid phase

The fluid fluxes do not require as much attention apart from the treatment of pressure $\hat{p}_f$. Usually, an interfacial pressure p_Γ appears in the multi-fluid model and is approximated by a combination of phase pressures. The modeling of this term depends on the application and is usually taken as $p_\Gamma = p_f$ for granular flows [22]. In the present solver, the interfacial pressure modeling comes from kinetic theory [16] and is treated separately as a buoyancy term. The 1-D problem for the fluid flux is then

$$\begin{aligned}
\partial_t\rho_f\alpha_f^\star &= -\partial_x\rho_f\alpha_f^\star u_f,\\
\partial_t\rho_f\alpha_f^\star u_f &= -\partial_x\cdot(\rho_f\alpha_f^\star u_f^2 + \hat{p}_f + P_{pfp}),\\
\partial_t\rho_f\alpha_f^\star E_f &= -\partial_x(\rho_f\alpha_f^\star u_f E_f + \alpha_f^\star u_f\hat{p}_f + \alpha_p^\star u_p\hat{p}_f + P_{pfp}u_p),\\
\partial_t\rho_f\alpha_f^\star k_f &= -\partial_x\cdot\rho_f\alpha_f^\star u_f k_f.
\end{aligned} \tag{88}$$

While the flux contains pressure, it does not correspond to a standard Euler step weighted by the volume fraction $\alpha_f^\star$. For this reason, the numerical scheme must be able to compute the reconstruction of pressure apart from the flux, which is not the case for the standard HLL scheme. Hence, the HLLC scheme is used to reconstruct the primitive variables $\mathbf{X}_f = (\rho_f, u_f, \hat{p}_f, E_f, k_f, P_{pfp})$. The slip pressure P_{pfp} is also included in the primitive variables of the fluid system as it appears in the momentum and energy fluxes and is required to compute buoyancy-like terms.

The HLLC scheme is a 3-wave approximate Riemann solver with four intermediate states such that

$$\mathbf{X}_f^{HLLC} = \begin{cases} \mathbf{X}_f^L, & \text{if } 0 \leqslant S^L; \\ \mathbf{X}_f^{L\star}, & \text{if } S^L \leqslant 0 \leqslant S^\star; \\ \mathbf{X}_f^{R\star}, & \text{if } S^\star \leqslant 0 \leqslant S^R; \\ \mathbf{X}_f^R, & \text{if } S^R \leqslant 0 \end{cases} \tag{89}$$

with $\mathbf{X}_f^K$ left ($K = L$) and right ($K = R$) states reconstructed at the face, and $\mathbf{X}_f^{K\star}$ the intermediate states at left and right side of the contact wave computed as detailed below. In the standard HLLC method, the left and right wave speed S^K are reconstructed as in HLL [13] or from the Roe-average [14]. In our solver, they are retrieved from the minimum and maximum eigenvalues of the fluid system eq. (88), which accounts for added-mass terms, and the contact wave speed $S^\star$ is computed as in [1]:

$$S^L = \lambda_{f,min}, \qquad S^R = \lambda_{f,max}, \qquad S^\star = \frac{\hat{p}_f^R - \hat{p}_f^L + \rho_f^L u_f^L (S^L - u_f^L) - \rho_f^R u_f^R (S^R - u_f^R)}{\rho_f^L (S^L - u_f^L) - \rho_f^R (S^R - u_f^R)}. \tag{90}$$

The contact pressure can then be computed as

$$\hat{p}_f^\star = \frac{1}{2}\left(\hat{p}_f^L + \hat{p}_f^R + \rho_f^L (S^L - u_f^L)(S^\star - u_f^L) + \rho_f^R (S^R - u_f^R)(S^\star - u_f^R)\right). \tag{91}$$

Finally, the left and right states apart from the contact wave can be computed as $\mathbf{X}_f^{K\star} = (\rho_f^{K\star}, S^\star, \hat{p}_f^\star, E_f^{K*}, k_f^{K\star}, P_{pfp}^K)$, such that

$$\rho_f^{K\star} = \rho_f^K \frac{S^K - u_f^K}{S^K - S^\star}, \qquad E_f^{K\star} = E_f^K + \frac{S^\star \hat{p}_f^\star - S^K \hat{p}_f^K}{\rho_f^K (S^K - u_f^K)}, \qquad k_f^{K\star} = k_f^K \frac{\rho_f^K}{\rho_f^{K\star}} \frac{S^K - u_f^K}{S^K - S^\star}. \tag{92}$$

The scheme results in an upwinding of the *pfp* pressure P_{pfp}. This is a key component of the method to ensure stability of the model as P_{pfp} is also discontinuous across a particle front. While the term is not significant in dense gas–particle systems, it needs to be treated carefully for bubbly flows.

To complete the fluid fluxes, the face volume fraction $\alpha_f^\star$ is reconstructed at the face from the particle fluxes:

$$\alpha_{f,i+\frac{1}{2}}^\star = \begin{cases} \alpha_{f,i+\frac{1}{2}}^{\star,L}, & \text{if } u_{p,i+\frac{1}{2}}^{1/2} \leqslant 0; \\ \alpha_{f,i+\frac{1}{2}}^{\star,R}, & \text{otherwise} \end{cases} \tag{93}$$

where $u_p^{1/2} = a_p^{1/2} \mathcal{M}_p^{1/2}$. The fluid fluxes are finally defined with $\mathbf{X}_f^{HLLC}$ at face $i + \frac{1}{2}$ such that

$$\mathbf{f}_{f,i+\frac{1}{2}} = \begin{pmatrix} \alpha_{f,i+\frac{1}{2}}^\star \rho_{f,i+\frac{1}{2}} u_{f,i+\frac{1}{2}} \\ \alpha_{f,i+\frac{1}{2}}^\star \rho_{f,i+\frac{1}{2}} u_{f,i+\frac{1}{2}} u_{f,i+\frac{1}{2}} + \hat{p}_{f,i+\frac{1}{2}} + P_{pfp,i+\frac{1}{2}} \\ \alpha_{f,i+\frac{1}{2}}^\star \rho_{f,i+\frac{1}{2}} E_{f,i+\frac{1}{2}} u_{f,i+\frac{1}{2}} + \alpha_{f,i+\frac{1}{2}}^\star u_{p,i+\frac{1}{2}}^{1/2} \hat{p}_{f,i+\frac{1}{2}} + u_{p,i+\frac{1}{2}}^{1/2} P_{pfp,i+\frac{1}{2}} \\ \alpha_{f,i+\frac{1}{2}}^\star \rho_{f,i+\frac{1}{2}} k_{f,i+\frac{1}{2}} u_{f,i+\frac{1}{2}} \end{pmatrix}. \tag{94}$$

In [27], the left and right reconstructions are performed with an optimized bandwidth version of WENO5 with non-linear error control [48] and a TVD slope limiter [28]. For a quantity Φ at face $i + \frac{1}{2}$ and its left-biased high-order

approximation $\Phi^{HO,L}_{i+\frac{1}{2}}$, the left reconstruction $\Phi^{L}_{i+\frac{1}{2}}$ is expressed as

$$\Phi^{L}_{i+\frac{1}{2}} = \Phi_i + 0.5\Delta x s_i^{TVD} \tag{95}$$

with the limited slope s_i^{TVD} defined as

$$s_i^{TVD} = \max\left[0, \min\left(2s_i^L, 2s_i^R, 2s_i^{HO}\right)\right], \qquad s_i^L = \frac{\Phi_i - \Phi_{i-1}}{\Delta x}, \qquad s_i^R = \frac{\Phi_{i+1} - \Phi_i}{\Delta x}, \qquad s_i^{HO} = \frac{\Phi^{HO,L}_{i+\frac{1}{2}} - \Phi_i}{\Delta x}. \tag{96}$$

In this work, the extension to higher order is done by employing HOUC5 reconstructions [40] instead. This high-order scheme is less dissipative than WENO5, but does not ensure boundedness. This last feature can be cured by employing an upwind scheme when overshoot or undershoot of the quantity occurs [26]. Here, the TVD slope limiter eq. (96) has shown to remove oscillations. This modification reduces significantly computational time as it does not require to compute non-linear sensors and adaptive stencils required for the WENO5 scheme at each time step.

4.2.3. Buoyancy-like exchange terms

Finally, the buoyancy-like terms contained in B are computed from the reconstructed particle and fluid quantities introduced above. The spatial discretization of $\partial_x \hat{p}_f$, F_{pf}, and $\partial_x P_{pfp}$ has to be done carefully to remain consistent with the HLLC fluxes. In practice, the face reconstructions defined in eq. (89) are used to compute B such that

$$\partial_x \hat{p}_f = \frac{\hat{p}_{f,1+\frac{1}{2}} - \hat{p}_{f,1-\frac{1}{2}}}{\Delta x},\ \partial_x \rho_f = \frac{\rho_{f,1+\frac{1}{2}} - \rho_{f,1-\frac{1}{2}}}{\Delta x},\ \partial_x u_f = \frac{u_{f,1+\frac{1}{2}} - u_{f,1-\frac{1}{2}}}{\Delta x},\ \partial_x P_{pfp} = \frac{P_{pfp,1+\frac{1}{2}} - P_{pfp,1-\frac{1}{2}}}{\Delta x}. \tag{97}$$

The extension to higher dimensions is straightforward employing directional splitting. Note that the curl velocity $\partial_{\mathbf{x}} \times \mathbf{u}_f$ related to the lift force is a 3-D operator that can also be computed from the reconstructed variables.

4.2.4. Time integration in hyperbolic step

The hyperbolic step is the only one treated explicitly. In order to remain stable with HOUC5 reconstructions, a RK3-SSP scheme is employed that also preserves realizability [51]. Given the hyperbolic step, eq. (74) is rewritten as

$$\partial_t \mathbf{Y} = \mathcal{H}(\mathbf{Y}), \tag{98}$$

and the time integration proceeds as follows [47]:

$$\begin{aligned} \mathbf{Y}^{(1)} &= \mathbf{Y}^n + \Delta t \mathcal{H}(\mathbf{Y}^n), \\ \mathbf{Y}^{(2)} &= \frac{3}{4}\mathbf{Y}^n + \frac{1}{4}\left(\mathbf{Y}^{(1)} + \Delta t \mathcal{H}(\mathbf{Y}^{(1)})\right), \\ \mathbf{Y}^{n+1} &= \frac{1}{3}\mathbf{Y}^n + \frac{2}{3}\left(\mathbf{Y}^{(2)} + \Delta t \mathcal{H}(\mathbf{Y}^{(2)})\right). \end{aligned} \tag{99}$$

As noted earlier, the overall time step is based on the maximum particle and fluid eigenvalues.

4.3. Numerical treatment of drag terms

Time splitting and a semi-analytical solution are used to update the drag terms in the 1-D momentum and energy balances, which amounts to solving the following system of ODEs:

$$\begin{aligned}
\partial_t \rho_f \alpha_f^\star &= 0 \\
\partial_t \rho_e \alpha_p^\star &= 0 \\
\partial_t \rho_f \alpha_f^\star u_f &= \frac{\rho_e \alpha_p^\star}{\tau_p}(u_p - u_f) \\
\partial_t \rho_e \alpha_p^\star u_p &= \frac{\rho_e \alpha_p^\star}{\tau_p}(u_f - u_p) \\
\partial_t \rho_f \alpha_f^\star k_f &= \frac{\rho_e \alpha_p^\star}{\tau_p}[3a\Theta_p - 2(1-a)k_f + u_{pf}^2 - C_f k_f] \\
\partial_t \rho_e \alpha_p^\star K_p &= -\frac{\rho_e \alpha_p^\star}{\tau_p}[3a\Theta_p - 2(1-a)k_f + u_{pf} u_p]
\end{aligned}
\quad \Longrightarrow \quad
\begin{aligned}
r &= \frac{\rho_e \alpha_p^\star}{\rho_f \alpha_f^\star} \\
\partial_t (u_f - u_p) &= -\frac{1+r}{\tau_p}(u_f - u_p) \\
\partial_t (u_f + r u_p) &= 0 \\
\partial_t k_f &= \frac{r}{\tau_p}[3a\Theta_p - 2(1-a)k_f] + \frac{r}{\tau_p}[u_{pf}^2(t) - C_f k_f] \\
\partial_t \Theta_p &= \frac{1}{\tau_p}\left[\frac{4}{3}(1-a)k_f - 2a\Theta_p\right]
\end{aligned}
\tag{100}$$

with r constant. The particle-phase internal energy e_p does not change due to drag, and the change in fluid-phase total energy $\rho_f \alpha_f^\star E_f$ is determined from conservation of total energy, i.e., $\rho_f \alpha_f^\star E_f + \rho_e \alpha_p^\star E_p$ is constant during drag. Note that the right-hand side for k_f has exchange terms and production/dissipation terms. In the following, we handle each part separately.

Holding τ_p constant over the time step, the updated phase velocities are approximated by

$$\begin{aligned}
u_f(t) - u_p(t) &= (u_f(0) - u_p(0))e^{-(1+r)t/\tau_p} \\
u_f(t) + r u_p(t) &= u_f(0) + r u_p(0)
\end{aligned}
\quad \Longrightarrow \quad
\begin{aligned}
u_f(t) &= \frac{u_f(0)}{1+r}(1 + re^{-(1+r)t/\tau_p}) + \frac{r u_p(0)}{1+r}(1 - e^{-(1+r)t/\tau_p}) \\
u_p(t) &= \frac{u_f(0)}{1+r}(1 - e^{-(1+r)t/\tau_p}) + \frac{u_p(0)}{1+r}(r + e^{-(1+r)t/\tau_p})
\end{aligned}
\tag{101}$$

and thus the source term for k_f is given by

$$u_{pf}^2(t) = u_{pf}^2(0)e^{-2(1+r)t/\tau_p}. \tag{102}$$

The evolution of $k_f(t)$ is written in two steps. First due to production and dissipation, it is written

$$\hat{k}_f = k_f(0)e^{-C_f r t/\tau_p} + \frac{r u_{pf}^2(0)}{2 + (2 - C_f)r}\left(e^{-C_f r t/\tau_p} - e^{-2(1+r)t/\tau_p}\right). \tag{103}$$

Second, the exchange terms form a linear system:

$$\partial_t \begin{bmatrix} k_f \\ \Theta_p \end{bmatrix} = -\frac{1}{\tau_p}\mathbf{A}\begin{bmatrix} k_f \\ \Theta_p \end{bmatrix} \qquad \text{where} \qquad \mathbf{A} = \begin{bmatrix} 2(1-a)r & -3ar \\ -\frac{4}{3}(1-a) & 2a \end{bmatrix}. \tag{104}$$

Since $0.5 \le a \le 1$, the two eigenvalues of $\mathbf{A}$ are non-negative: $\lambda_1 = 0$ and $\lambda_2 = 2r(1-a) + 2a$. Hence, the solution is

$$\begin{aligned}
k_f(t) &= \frac{1}{\lambda_2}\left[2r(1-a)\hat{k}_f e^{-\lambda_2 t/\tau_p} + 2a\hat{k}_f + 3ra\Theta_p(0)(1 - e^{-\lambda_2 t/\tau_p})\right], \\
\Theta_p(t) &= \frac{1}{\lambda_2}\left[2r(1-a)\Theta_p(0) + 2a\Theta_p(0)e^{-\lambda_2 t/\tau_p} + \frac{4}{3}(1-a)\hat{k}_f(1 - e^{-\lambda_2 t/\tau_p})\right].
\end{aligned}
\tag{105}$$

Note that $2k_f(t) + 3r\Theta_p(t) = 2\hat{k}_f + 3r\Theta_p(0)$ is constant for the exchange terms, and the parameter a fixes the steady-state value of k_f.

The collisional, frictional, and heat-transfer terms are handled in the same manner as the drag terms. For each term, a separate semi-analytical solution is derived and used to update the conserved variables in each phase. In this

Table 4: Default physical properties of the fluids used for test cases.

Fluid	γ_f	$p_{\infty,f}$ (GPa)	ν_f (Pa·s)	$C_{p,f}$ (J/kg/K)	λ_f (m^2/s)
Air	1.4	0	$2.12 \cdot 10^{-5}$	1005	$2.56 \cdot 10^{-2}$
Water	4.4	0.6	$1 \cdot 10^{-6}$	5250	$6 \cdot 10^{-2}$

manner, strict conservation of mass, momentum, and total energy is enforced at every time step. The extension to 3-D flows is done analogously.

4.4. Numerical treatment of added-mass source terms

Time splitting and a semi-analytical solution are used to handle the 1-D added-mass source terms. For the particle phase, this amounts to solving a linear system of ODEs:

$$\begin{aligned} \partial_t \rho_e \alpha_p^\star &= C_\xi \rho_e \alpha_p^\star \\ \partial_t \rho_e \alpha_p^\star e_p &= C_u e_f \rho_e \alpha_p^\star + (C_\xi - C_u)\rho_e \alpha_p^\star e_p \\ \partial_t \rho_e \alpha_p^\star u_p &= C_u u_f \rho_e \alpha_p^\star + (C_\xi - C_u)\rho_e \alpha_p^\star u_p \\ \partial_t \rho_e \alpha_p^\star K_p &= C_u K_f \rho_e \alpha_p^\star + (C_\xi - C_u)\rho_e \alpha_p^\star K_p \end{aligned} \quad \Longrightarrow \quad \begin{aligned} \partial_t \rho_e \alpha_p^\star &= C_\xi \rho_e \alpha_p^\star \\ \partial_t e_p &= C_u(e_f - e_p) \\ \partial_t u_p &= C_u(u_f - u_p) \\ \partial_t K_p &= C_u(K_f - K_p) \end{aligned} \tag{106}$$

with e_f, u_f, K_f, C_ξ, and C_u held constant. The analytical solution for the mass at time t is

$$(\rho_e \alpha_p^\star)(t) = (\rho_e \alpha_p^\star)(0)\, e^{C_\xi t}. \tag{107}$$

The change of mass in the fluid phase over the time step Δt is then $(\rho_e \alpha_p^\star)(0) - (\rho_e \alpha_p^\star)(\Delta t)$. For the internal energy, momentum, and kinetic energy, the analytical solutions are

$$e_p(t) = e_p(0)e^{-C_u t} + e_f\left(1 - e^{-C_u t}\right), \tag{108}$$

$$u_p(t) = u_p(0)e^{-C_u t} + u_f\left(1 - e^{-C_u t}\right), \tag{109}$$

$$K_p(t) = K_p(0)e^{-C_u t} + K_f\left(1 - e^{-C_u t}\right). \tag{110}$$

The change in momentum and total energy in the fluid phase are computed in the same manner as for mass. The extension to 3-D flows is done analogously.

5. Numerical examples

This section consists of various 1-D test cases to assess the solver's capabilities to handle a large range of Mach numbers, volume fractions, and material-density ratios between the fluid and particles. For this purpose, the fluid can be either air or water with properties given in table 4. The particle phase can be solid particles or non-deformable spherical bubbles with properties provided in the corresponding test case. In the solver, the minimum value of the particle-phase volume fraction α_ϵ is set at a small value (10^{-12}) to avoid division by zero. Therefore, the quantities for the disperse phase are only displayed when $\alpha_p > 10^{-8}$ to provide meaningful values. In all test cases, if not specified, the model parameters take the values $e_c = 1$, $\Delta_f = 0.01$, $\alpha_{max} = 0.65$ and $C_{pfp} = 0.2$ and the CFL number takes the value of 0.5.

In general, for gas–particle test cases, the model formulation, numerical solver, and results are very similar to [27]. In contrast, the bubbly flow cases are more challenging for the hyperbolic solver because of the strong phase coupling due to buoyancy and added mass. Unlike for gas–particle flows wherein the largest eigenvalues can arise in the particle phase, this does not occur for bubbly flows. Nonetheless, complex eigenvalues are likely to arise in bubbly flow due to buoyancy when the *pfp* pressure P_{pfp} is too small,leading to nonphysical behavior of the two-fluid model [20]. For the model proposed in this work, this behavior is avoided if $C_{pfp} \geq 0.5$.

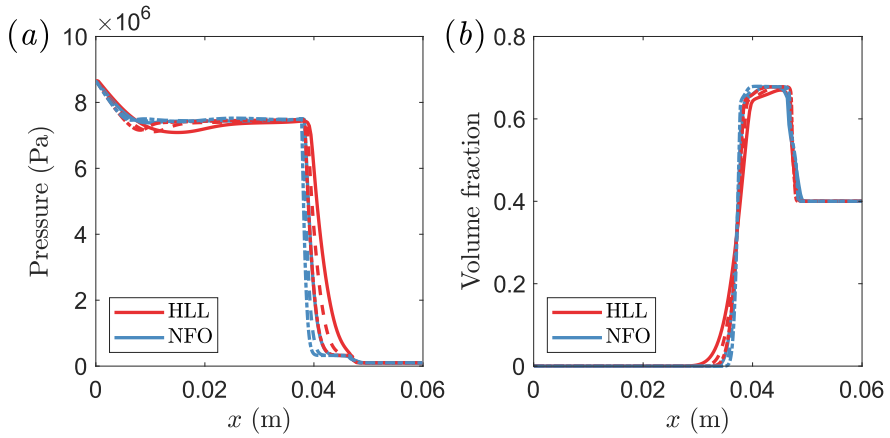

Figure 2: Gas-phase pressure (a) and particle volume fraction (b) for the dense shock tube case at $t = 100$ µs using HLL (red) and NFO (blue). The three levels of grid refinement are $N_x = 200$ (——), 400 (- - -) and 800 (-···-).

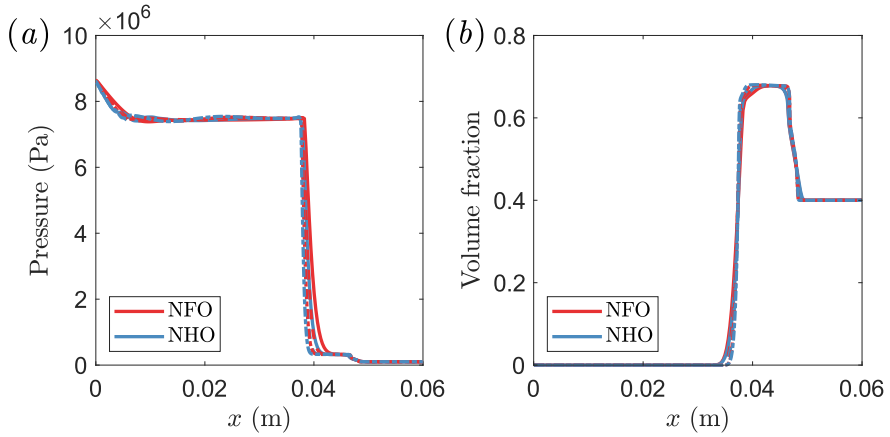

Figure 3: Gas-phase pressure (a) and particle volume fraction (b) for the dense shock tube case at $t = 100$ µs using NFO (red) and NHO (blue). The three levels of grid refinement are $N_x = 200$ (——), 400 (- - -) and 800 (-···-).

5.1. Validation of the hyperbolic solver

First, the proposed computational scheme is compared to the first-order HLL scheme employed in [20]. A first-order version of the present scheme is also studied to compare the features of the schemes setting aside the order of reconstruction of the quantities. The first-order version of the scheme then uses Euler integration in time and upwind reconstructions for both phases. The first-order and high-order versions of the new scheme will be referred as NFO and NHO, respectively. The validation test case is taken from [27] where a strong shock interacts with a dense particle cloud. It consists of a shock tube where the left chamber contains pure high-pressure air, while the right chamber is filled with a mixture of air and particles.

The particle concentration is chosen to be high, such that the volume fraction front approaches the packing limit as the shock pushes the particle phase to the right of the domain. The method should be able to remain stable when P_f controls the eigenvalues. Moreover, the strong shock creates a sudden heating of the gas that is partially absorbed by the particle phase, which has the effect of highly weakening the shock. The computational domain length is $L = 0.06$ m, and the left and right states are separated by a diaphragm located at $x = 0.03$ m. Solid particles are defined with $\rho_p = 1470$ kg/m^3, $d_p = 5$ µm, and $C_{V,p} = 987$ J/kg/K. The left and right states for the gas are $p_f^L = 100$ atm, $p_f^R = 1$ atm, $T_{f,p}^L = T_{f,p}^R = 300$ K, $\alpha_f^L = 1$, and $\alpha_f^R = 0.6$. The three schemes are compared for three levels of grid refinement: $N_x = 200$, 400, and 800.

The fluid pressure and particle volume fraction at $t = 100$ µs are shown in fig. 2 for HLL versus NFO, and in

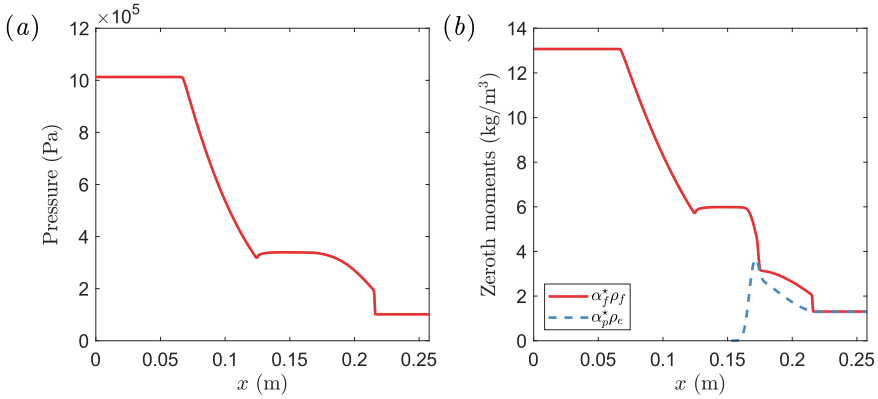

Figure 4: Gas-phase pressure (*a*) and mass densities (*b*) for the dilute shock tube at $t = 184$ µs.

fig. 3 for NFO versus NHO. It is clear from both the pressure and volume fraction that the new scheme combining AUSM$^+$up and HLLC is better at capturing discontinuities. Even though first-order reconstructions are used, the new scheme is able to capture the particle front accurately. More quantitatively, the HLL scheme requires $N_x = 800$ to give the same degree of details compared to NFO with $N_x = 200$ on this test case. In comparison, the higher-order reconstructions allow to better capture the pressure discontinuities, while no substantial differences can be observed for the particle front. This can be explained by the first-order upwind reconstructions used in the AUSM$^+$up scheme for both NFO and NHO.

Interestingly, using higher-order reconstructions has less impact on the results than using AUSM$^+$up and HLLC instead of HLL. This is partly due to the lack of complex fluid structures in 1-D, which would better showcase the impact of using higher-order reconstructions [27]. Overall, all the schemes converge with mesh refinement. Now that the proposed scheme has been validated and mesh convergence has been assessed on a demanding test case, the remaining numerical examples are computed using the high-order scheme NHO and the highest mesh refinement: $N_x = 800$.

5.2. Air shock wave interacting with a particle cloud

In this example, a dilute shock tube and the dense shock tube presented above are investigated. In general, gas–particle flows are simpler to simulate than bubbly flows due to relatively small effect of buoyancy. However, due to differences in the model formulation (e.g., the frictional source and slip-pressure tensor), results from the two-fluid model in table 1 can be expected to exhibit some differences with the model in [27] for gas–particle flows.

5.2.1. Dilute shock tube

In this shock tube, the right state contains a very dilute particle phase such that the solver must handle an almost pressure-less system. The domain length is $L = 0.257798$ m and the left and right states are separated by a diaphragm located at $x = 0.129$ m to reproduce the same setup as in [27]. Even though no exact solution exists for this case, results can be compared to the results presented in [27]. Solid particles are defined with $\rho_p = 2500\,\mathrm{kg/m^3}$, $d_p = 10\,\mu\mathrm{m}$, and $C_{V,p} = 720$ J/kg/K. The left and right states are $p_f^L = 10$ atm, $p_f^R = 1$ atm, $T_{f,p}^L = T_{f,p}^R = 270$ K, $\alpha_p^L = 0$, and $\alpha_p^R = 5.172 \cdot 10^{-4}$. The quantities of interest are plotted at $t = 184$ µs in fig. 4. While the shock is progressing in the gas–particle mixture, it experiences momentum and heat loss because of drag forces. As noted in [27], the hook-like structure of $\hat{p}_f$ near the initial shock position is well captured. The main difference with [27] is the profile of particle mass density near $x = 0.15$, which is higher with our model. This is likely due to the unsteady force $\mathbf{F}_{pf}$ that accelerates the particles near the shock and contact surface. Overall, the physical behavior is retrieved and showcases the performance of the proposed scheme near pressure-less conditions.

5.2.2. Dense shock tube

The problem introduced in section 5.1 is repeated with more details to better describe the weakening of the shock, the balance of particle pressure in the dense part of the granular phase, and the effect of drag on phase velocities. In

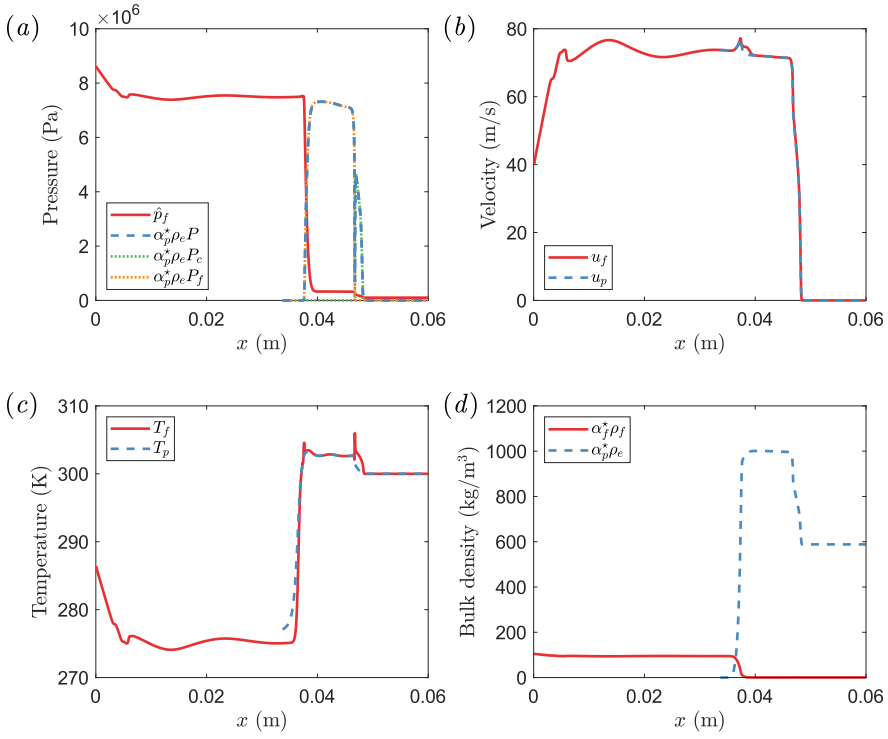

Figure 5: Pressures (*a*), velocities (*b*), temperatures (*c*), and mass densities (*d*) for the dense shock tube at $t = 1$ ms.

Table 5: Physical properties of the fluid and particle phases for particle-curtain cases.

Configuration	Material	ρ_p (kg/m^3)	d_p (µm)	δ_0 (mm)	α_p	$\mathcal{M}_s$
1	316 stainless steel	8170	115	1.7	0.17	1.4
2	Tungsten	17070	115	2.3	0.18	1.55
3	Cast stainless steel	7390	328	4.0	0.09	1.7
4	Soda lime glass	2420	115	2.0	0.19	4.24

fig. 5, the phase pressures, velocities, temperatures and mass densities are provided. The solutions agree well with [27], apart from the granular pressure which experiences an abrupt decrease at the particle front. By plotting the collisional and frictional parts of the particle pressure (which are clearly separated at $\alpha_p = \alpha_{max}$), it can be seen that the frictional pressure is controlling where the volume fraction approaches the packing limit, but decreases abruptly at the particle front. This behavior is due to the different functional forms used for the frictional pressure in the present model compared to what was used in [27]. By increasing the parameter Δ_f, the transition zone is larger and frictional pressure is applied at lower volume fractions. The temperature profiles showcase the heating of particles through the shock, which explains the weakening of the shock with an amount equivalent to what was observed in [27].

Finally, it is interesting to notice that the present model is stable and without particle-pressure oscillations, even when $e_c = 1$. In [27], strong oscillations were observed and additional dissipation was needed in the numerical scheme to control them. In the current model, the granular temperature Θ_p is strongly damped to negligible values in the frictional regime by the frictional source term included in H_p. Moreover, we use a sharper cut-off between the frictional and collisional regimes in the definition of P_f (see individual particle pressure contribution in fig. 5(a)), and compute the particle-phase eigenvalues directly from the Jacobian matrix. As a result, the proposed hyperbolic solver is robust with $e_c = 1$ without additional dissipation even when $\alpha_p > \alpha_{max}$.

5.3. Shock-induced dispersal of particle curtains

Next, the gas–particle solver is validated against experimental data. The most commonly used experiment is the interaction of a shock with a particle curtain. Usually solutions are compared with the famous experiment of Rogue et al. [44]. Here, the recent experiments of Daniel et al. [9] are reproduced with volume fraction ranging from $\alpha_p = 0.09$ to $\alpha_p = 0.2$, Mach number of the air shock ranging from $\mathcal{M}_f = 1.4$ to $\mathcal{M}_f = 1.7$, and four different particles with variable density and diameter. A recent hypersonic configuration with $\mathcal{M}_f = 4.24$ from the same group [52] is also simulated. The four configurations are summarized in table 5.

The computational domain is $[-L/2, L/2]$ with $L = 0.2$ m and non-reflective boundary conditions are used to imitate the experiments. The shock is produced by a pressure ratio with the diaphragm located upstream of the curtain at $x_d = -L/4$. The pressure ratio between driver (state 2) and driven (state 1) chambers are related to the shock Mach number $\mathcal{M}_s$:

$$\frac{p_2}{p_1} = \frac{1 + \frac{2\gamma_1}{\gamma_1+1}\left(\mathcal{M}_s^2 - 1\right)}{(1 - \frac{\gamma_2-1}{\gamma_1+1}\frac{c_1}{c_4}\frac{\mathcal{M}_s^2-1}{\mathcal{M}_s})^{\frac{2\gamma_2}{\gamma_2-1}}}. \tag{111}$$

The driver gas is not expected to be relevant for the interaction with the curtain and has been taken as air, while nitrogen was used in the experiments [9]. The driven air is at ambient conditions $T_1 = 297$ K and $p_1 = 84.1$ kPa. The driver air temperature is also taken at $T_2 = 297$ K. Example results obtained with the solver are represented in fig. 6a where an x-t diagram of density with isocontours of α_p are plotted. When the diaphragm is released, a contact wave and a shock wave are created and propagate towards the curtain. The time is defined such that $t = 0$ represents the moment where the shock wave hits the upstream edge of the curtain. Then a part of the shock wave is transmitted, while a reflected shock wave travels back upstream. Complex patterns are then generated by the combination of the initial contact wave and reflected shock wave.

The spread rate is compared with the experiments where all four configurations are displayed in fig. 6b. It can be observed that the results fairly compare with the experiments, but with deviations when the Mach number increases. This can hide an underlying relation between drag and Mach number, which can be modeled for hard spheres [36]. A detailed study of the effect of the drag model on the physical behavior of the particles is outside the scope of this paper.

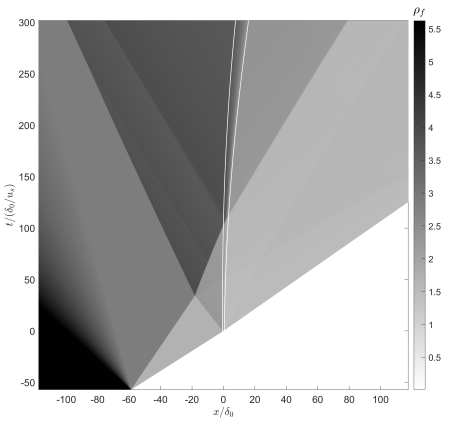

(a) x-t diagram of density with isocontours of α_p (white) for configuration 1.

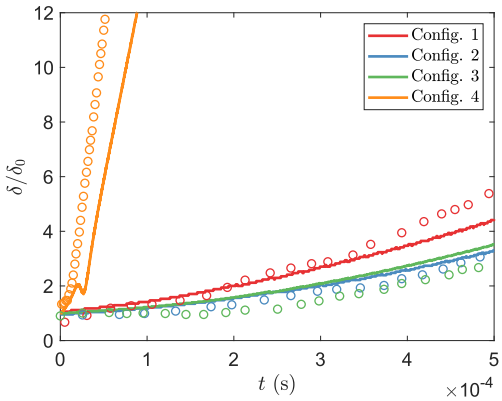

(b) Comparison of the results obtained by the experiment (symbols) and the numerical results (solid lines) for the four configurations detailed in table 5.

Figure 6: Shock-induced dispersal of particle curtains illustrated with the x-t diagram of density (left) and the comparison of the spread rate with experimental data (right).

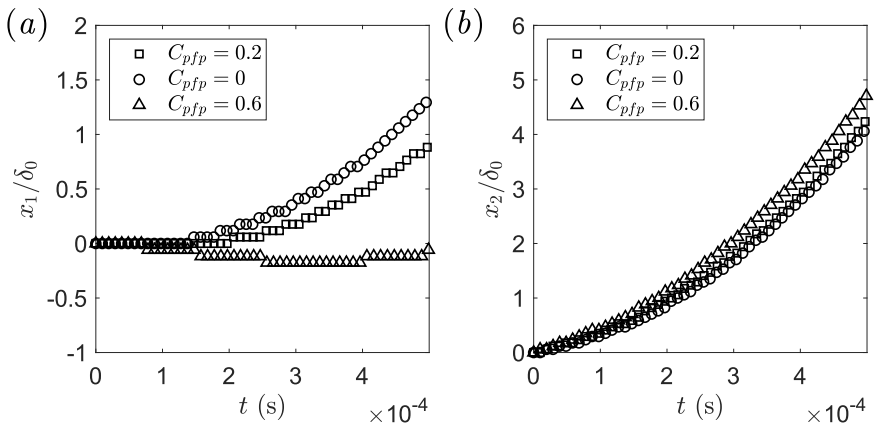

Figure 7: Comparison of upstream edge position x_1 (a) and downstream edge position x_2 (b) for different values of C_{pfp} in configuration 1.

Table 6: Two configurations from [2] tested for a water shock in a fixed particle array. τ corresponds to the transit time d_p/u_s.

Configuration	$\mathcal{M}_s$	α_p	p_f^L (MPa)	ρ_f^L (kg/m^3)	u_f^L (m/s)	τ (ns)
LM10	1.22	0.1	477.73	1136.1	241.2	50.39
HM20	3	0.2	7823.7	1487.8	1606.5	20.49

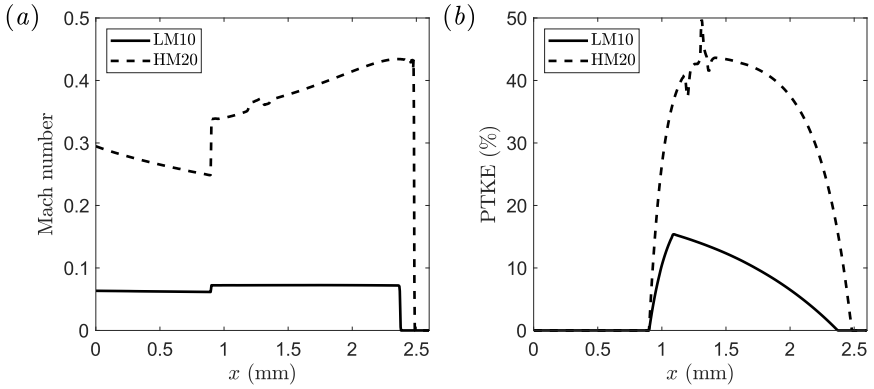

Figure 8: Mach number (a) and PTKE (b) for the two configurations LM10 and HM20 at $t = 16\tau$.

Another explanation for the difference between the numerical and experimental results can be due to the value of C_{pfp}, which has been taken equal to 0.2. This coefficient controls the magnitude of the *pfp* pressure, which can have a strong implication on the spreading of the particles in the curtain, especially for high Mach numbers with large slip velocity. To investigate this model parameter, the first configuration has been simulated with different values of C_{pfp} ranging from 0 to 0.6 and the related spread rates are plotted in fig. 7. The results illustrate the impact of C_{pfp} on the granular phase dynamics. When the *pfp*-pressure magnitude is increased using C_{pfp}, the upstream edge position x_1 is highly impacted. The curtain can even go backward in the case of $C_{pfp} = 0.6$, while the upstream edge does not move as much when C_{pfp} is set to 0. For the downstream edge location x_2, the difference is not as significant and all three curves almost collapse.

5.4. Underwater shock wave in a fixed particle array

Now that gas–particle systems have been investigated, the interaction of an underwater shock with fixed particles is considered. The main particularity of a water shock compared to a gas shock is that the resulting post-shock Mach number is subsonic. The set-up is based on the DNS study presented in [2] where a random array of fixed particles is defined in a part of the domain and a strong shock is initialized upstream of the array. In the model, the particle density is fixed at $\rho_p = 10^9$ kg/m^3 to make sure that the granular phase remain fixed. However, $\alpha_p^\star$ is still able to vary because of the added mass. The mean particle diameter is $d_p = 100$ µm and heat transfer is deactivated as in the DNS. The domain is taken as $L = 26d_p$, while the particle array is located at $x_p = 9d_p$ and extends until the right end of the domain. The shock is initially positioned one diameter before the particle array $x_s = 8d_p$.

In [2], two Mach numbers and volume fractions are simulated, leading to four configurations. Here, the two configurations, referred as LM10 and HM20, are tested and compared to the DNS results. The volume fraction and post-shock (left) state corresponding to the two configurations are summarized in table 6. The pre-shock (right) state is defined as $p_f^R = 1$ atm, $\rho_f^R = 998.0$ kg/m^3. The simulations stop at $t = 16\tau$ with $\tau = d_p/u_s$ the transit time. In the simulations, large fluctuations of the fluid velocity (corresponding to PTKE) can be observed for HM20, while only small interactions with the particle array are observed for LM10. To compare with the DNS results, the Mach number u_f/a_f and dimensionless PTKE $2k_f/u_f^2$ are shown in fig. 8.

The velocity fluctuations correspond to PTKE in the model and are well reproduced in the 1-D simulation wherein dimensionless PTKE reaches 50% for HM20. The results compare well with the Mach contour provided in [2] where reflections are only observed for HM20. In fig. 9, the volume fractions of pure particle phase α_p and particle with added mass $\alpha_p^\star$ are also presented. It is interesting to notice that α_p remains constant, as particle material density is

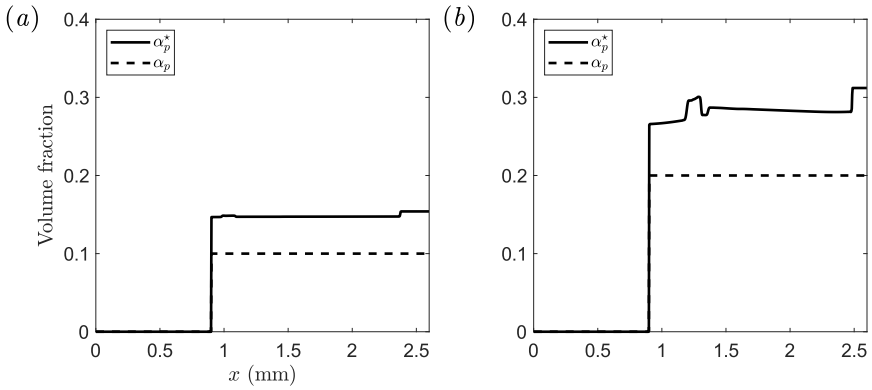

Figure 9: Volume fractions α_p and $\alpha_p^\star$ for the two configurations LM10 (a) and HM20 (b) for at $t = 16\tau$.

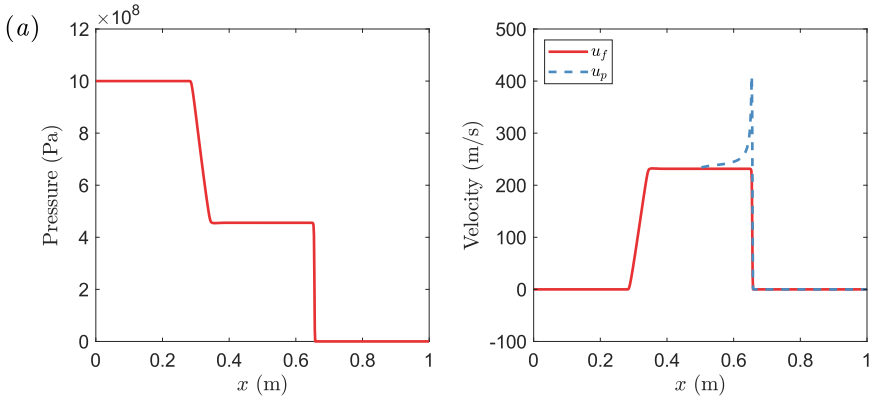

Figure 10: Fluid pressure (a) and phase velocities (b) for low aeration at $t = 79$ µs.

very high. However, $\alpha_p^\star$ increases in the particle phase as a result of fluid-density variations. This added-mass rise has an impact on the mean and fluctuating velocities of the fluid. Indeed, a bump of Mach and a spike in PTKE can be observed in fig. 8 at the exact location where added-mass increases. This illustrates the effects of added mass even for a case where the particles are fixed. The predicted magnitude of this effect can be modified using the parameter C_a in the definition of τ_a.

5.5. Shock wave in a bubbly flow

The final numerical example is adapted from the shock tube test cases of section 5.2, but the fluid is water and the particle phase has a low material density such that it mimics non-deform-able spherical bubbles. The domain length is $L = 1$ m and the left and right states are separated by a diaphragm located at $x = 0.5$ m to reproduce the same setup as in [21]. Particles are defined with $\rho_p = 1$ kg/m^3, $d_p = 500$ µm, and $C_{V,p} = 987$ J/kg/K. The left and right states are taken as $p_f^L = 10^9$ Pa, $p_f^R = 10^5$ Pa, $\rho_f^L = \rho_f^R = 1000$ kg/m^3. The left state is pure water, while the right state corresponds to a bubbly flow with different aeration levels α_p^R. Note that a proper bubble model would use a bubble pressure to determine the bubble diameter and material density. Nevertheless, the setup is still relevant to show the capability of the solver to handle large material-density ratios between the fluid and particles, and the resultant slip velocity. In such systems, the buoyancy terms become important and hyperbolicity is only preserved thanks to the slip-pressure tensor [20]. For this reason, the C_{pfp} coefficient needs to be at least 0.5 to preserve hyperbolicity of the two-fluid model [20].

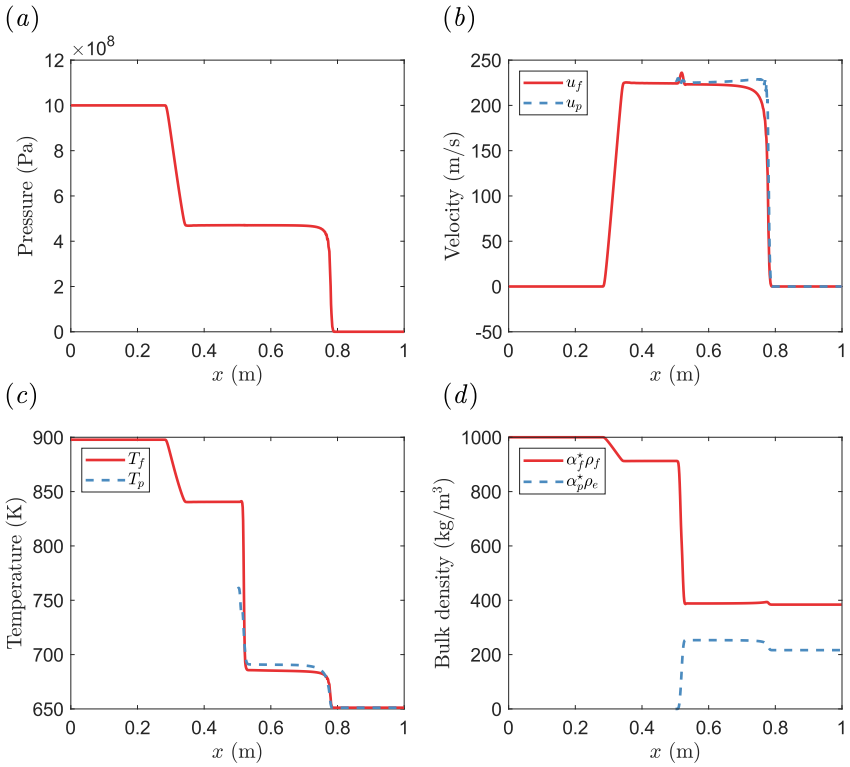

Figure 11: Fluid pressure (*a*), velocities (*b*), temperatures (*c*), and mass densities (*d*) for high aeration at $t = 79$ µs.

5.5.1. Low aeration

As done for the gas–particle system, a first test is defined with a low volume fraction of $\alpha_p^R = 10^{-4}$. The pressure and phase velocities at $t = 79$ µs are displayed in fig. 10. As expected, the bubble swarm is too dilute to impact the water shock. The shock wave then crosses the bubble swarm without decelerating. From the velocity profiles, it is interesting to notice that the slip velocity is especially large compared to the gas–particle systems. This is due to the predominant buoyancy-like terms in bubbly flows. At the shock front, the pressure gradient is very large and creates a strong acceleration of the bubble swarm. The bubble velocity subsequently relaxes back to the fluid velocity behind the shock due to drag. Similar, but not as strong, behavior is observed for smaller bubbles. As expected, the predicted values of Θ_p are small in bubbly flows due to the small Stokes number.

5.5.2. High aeration

In this case, the same setup is used with a volume fraction of $\alpha_p^R = 0.4$. The fluid pressure, phase velocities, temperatures and mass densities at $t = 79$ µs are displayed in fig. 11. In opposition to the gas–particle dense case, the shock is not weakened by the dense bubble swarm. On the contrary, it is accelerated because of the reduction of cross section experienced by water as α_p increases. However, the same velocity peak observed in gas–particle flows appears at the upstream edge of bubble swarm. Finally, the pressure gradient is smoothed at the shock front, which does not produce an acceleration comparable to the dilute case. As a result, the bubble volume fraction does not increase significantly as was observed for the heavy particles. This last test case demonstrates the capability of the solver to simulate water–bubble systems where added mass and buoyancy-like terms are predominant. In gravity-driven systems, large volume-fraction regions (e.g., foams) can be produced, leading to a frictional-pressure contributions. However, such flow dynamics occur on much longer time scales than the shock waves investigated here.

6. Conclusions

In this work, a hyperbolic two-fluid model for high-speed, fully compressible, monodisperse fluid–particle flows with added mass and fluid-phase pseudoturbulence has been developed and tested. The particle-phase equations have been derived from a kinetic model with terms for the collisional, frictional, and *pfp*-pressure contributions to the particle pressure, accounting as well for the particle-phase internal energy to capture heat transfer with the fluid phase. For simplicity, only velocity moments up to second order are considered, which is valid for collisional and/or low-Stokes-number flows.

For the numerical solver, the resulting nine-equation two-fluid model was discretized with a higher-order method along the lines of the pioneering work of [27]. The main issue was to adapt the combination of AUSM$^+$up and HLLC initially proposed in the context of a seven-equation two-fluid model to the present model without loss of robustness. This has been done by treating carefully the additional buoyancy-like terms with a consistent discretization. Moreover, the complex coupling of particle- and fluid-phase quantities through the added mass was treated by computing the eigenvalues directly from the Jacobian of the spatial fluxes.

The first numerical study assessed the solver on a challenging gas–particle test case, including a granular phase reaching the packing limit and a strong shock in the fluid phase. The advantages of the proposed method have been showcased in comparison to the first-order HLL scheme used in [20]. Then, the numerical examples presented in the results section demonstrate the capability of the numerical solver to handle a wide range of two-phase systems from supersonic to hypersonic flows, dilute-to-dense granular phases, and gas–particle to bubbly flows. Generally speaking, the proposed model is able to reproduce the global behavior of DNS and experiments in the literature.

In future work, the two-fluid model and numerical scheme developed in this work could be extended in several directions. For example, to handle reacting flows, chemical species in the fluid and particle phases can be modeled as done in [27, 28]. Another interesting and important improvement would be to include polydispersity of the particle phase along the lines of the kinetic model developed in [31] and using quadrature-based moments methods for the numerical solver [37]. Finally, in order to simulate the numerous applications involving low-speed, low-Mach-number flows with mean shear, it would be useful to develop a low-Mach-number solver for the proposed two-fluid model that neglects the acoustic waves in the fluid phase [41]. For such applications, it will be necessary to include constitutive relations for the viscous and thermal fluxes [3, 6, 7, 29], which have no effect on the hyperbolicity of the two-fluid model [20]. These additions would allow the proposed two-fluid model to be used for gravity-driven and/or pressure-driven multiphase flows such as bubble columns, sedimentation, and fluidized beds.

Acknowledgments

When preparing this work, ROF was supported by the 2022-2023 Fulbright–Tocqueville Distinguished Chair Award. The Government of the United States or any agency representing it has not endorsed the conclusions or approved the contents of this publication.

References

[1] P. Batten, N. Clarke, C. Lambert, and D. M. Causon. On the choice of wavespeeds for the HLLC Riemann solver. SIAM Journal on Scientific Computing, 18(6):1553–1570, 1997.

[2] J. Behrendt, S. Balachandar, and T. P. McGrath. Shock interacting with a random array of stationary particles underwater. Physical Review Fluids, 7(2):023401, 2022.

[3] D. Berzi, J. T. Jenkins, and P. Richard. Extended kinetic theory for granular flow over and within an inclinded erodible bed. Journal of Fluid Mechanics, 885:A27, 2020.

[4] P. L. Bhatnagar, E. P. Gross, and M. Krook. A model for collision processes in gases. I. Small amplitude processes in charged and neutral one-component systems. Physical Review, 94(3):511, 1954.

[5] J. Capecelatro. Modeling high-speed gas–particle flows relevant to spacecraft landings. International Journal of Multiphase Flow, 150:104008, 2022.

[6] J. Chauchat. A comprehensive two-phase flow model for unidirectional sheet-flows. Journal of Hydraulic Research, 56:15, 2018.

[7] J. Chauchat and M. Médale. A three-dimensional numerical model for dense granular flows based on the $\mu(I)$ rheology. Journal of Computational Physics, 256:696–712, 2014.

[8] T. L. Cook and F. H. Harlow. Virtual mass in multiphase flow. International Journal of Multiphase Flow, 10(6):691–699, 1984.

[9] Kyle A. Daniel and Justin L. Wagner. The shock-induced dispersal of particle curtains with varying material density. International Journal of Multiphase Flow, 152:104082, 2022.

[10] S. L. Davis, T. B. Dittmann, G. B. Jacobs, and W. S. Don. Dispersion of a cloud of particles by a moving shock: Effects of the shape, angle of rotation, and aspect ratio. Journal of Applied Mechanics and Technical Physics, 54:900–912, 2013.
[11] Edward P. DeMauro, Justin L. Wagner, Lawrence J. DeChant, Steven J. Beresh, and Aaron M. Turpin. Improved scaling laws for the shock-induced dispersal of a dense particle curtain. Journal of Fluid Mechanics, 876:881–895, 2019.
[12] A. Di Benedetto, P. Russo, P. Amyotte, and N. Marchand. Modelling the effect of particle size on dust explosions. Chemical Engineering Science, 65(2):772–779, 2010.
[13] B. Einfeldt. On Godunov-type methods for gas dynamics. SIAM Journal on Numerical Analysis, 25(2):294–318, 1988.
[14] B. Einfeldt, C.-D. Munz, P. L. Roe, and B. Sjögreen. On Godunov-type methods near low densities. Journal of Computational Physics, 92(2):273–295, 1991.
[15] R. O. Fox. On multiphase turbulence models for collisional fluid–particle flows. Journal of Fluid Mechanics, 742:368–424, 2014.
[16] R. O. Fox. A kinetic-based hyperbolic two-fluid model for binary hard-sphere collisions. Journal of Fluid Mechanics, 877:282–329, 2019.
[17] R. O. Fox. Advanced approaches in turbulence: Theory, modeling, simulation, and data analysis for turbulent flows, chapter Multiphase turbulence, pages 307–372. Elsevier, Amsterdam, Netherlands, 2021.
[18] R. O. Fox and F. Laurent. Hyperbolic quadrature method of moments for the one-dimensional kinetic equation. SIAM Journal on Applied Mathematics, 82(2):750–771, 2022.
[19] R. O. Fox, F. Laurent, and A. Vié. Conditional hyperbolic quadrature method of moments for kinetic equations. Journal of Computational Physics, 365:269–293, 2018.
[20] R. O. Fox, F. Laurent, and A. Vié. A hyperbolic two-fluid model for compressible flows with arbitrary material-density ratios. Journal of Fluid Mechanics, 903:A5, 2020.
[21] Damien Furfaro and Richard Saurel. A simple HLLC-type Riemann solver for compressible non-equilibrium two-phase flows. Computers & Fluids, 111:159–178, 2015.
[22] D. Gidaspow. Multiphase Flow and Fluidization: Continuum and Kinetic Theory Descriptions. Academic Press, New York, USA, 1994.
[23] Sigal Gottlieb, Chi-Wang Shu, and Eitan Tadmor. Strong stability-preserving high-order time discretization methods. SIAM Review, 43(1):89–112, 2001.
[24] Hervé Guillard and B. Nkonga. On the behaviour of upwind schemes in the low Mach number limit: A review. Handbook of Numerical Analysis, 18:203–231, 2017.
[25] D. J. Gunn. Transfer of heat or mass to particles in fixed and fluidized beds. International Journal of Heat and Mass Transfer, 21:467–476, 1978.
[26] Marcus Herrmann, Guillaume Blanquart, and Venkat Raman. Flux corrected finite volume scheme for preserving scalar boundedness in reacting large-eddy simulations. AIAA journal, 44(12):2879–2886, 2006.
[27] R. W. Houim and E. S. Oran. A multiphase model for compressible granular–gaseous flows: formulation and initial tests. Journal of Fluid Mechanics, 789:166–220, 2016.
[28] Ryan W. Houim and Kenneth K. Kuo. A low-dissipation and time-accurate method for compressible multi-component flow with variable specific heat ratios. Journal of Computational Physics, 230(23):8527–8553, 2011.
[29] J. T. Jenkins and M. Larcher. Dense, steady, fully developed fluid-particle flows over inclined, erodible beds. Physical Review Fluids, 8:024303, 2023.
[30] B. Kong and R. O. Fox. A solution algorithm for fluid–particle flows across all flow regimes. Journal of Computational Physics, 344:575–594, 2017.
[31] B. Kong and R. O. Fox. A moment-based kinetic theory model for polydisperse gas–particle flow. Powder Technology, 365:92–105, 2020.
[32] Y. Ling, J. L. Wagner, S. J. Beresh, S. P. Kearney, and S. Balachandar. Interaction of a planar shock wave with a dense particle curtain: Modeling and experiments. Physics of Fluids, 24(11):113301, 2012.
[33] M.-S. Liou. A sequel to AUSM: AUSM$^+$. Journal of Computational Physics, 129(2):364–382, 1996.
[34] M.-S. Liou. A sequel to AUSM, Part II: AUSM$^+$-up for all speeds. Journal of Computational Physics, 214(1):137–170, 2006.
[35] M.-S. Liou and C. J. Steffen Jr. A new flux splitting scheme. Journal of Computational Physics, 107(1):23–39, 1993.
[36] Eric Loth, John Tyler Daspit, Michael Jeong, Takayuki Nagata, and Taku Nonomura. Supersonic and hypersonic drag coefficients for a sphere. AIAA Journal, 59(8):3261–3274, 2021.
[37] D. L. Marchisio and R. O. Fox. Computational Models for Polydisperse Particulate and Multiphase Systems. Cambridge University Press, Cambridge, UK, 2013.
[38] T. McGrath, J. St. Clair, and S. Balachandar. Modeling compressible multiphase flows with dispersed particles in both dense and dilute regimes. Shock Waves, 28:533–544, 2018.
[39] M. Mehrabadi, S. Tenneti, R. Garg, and S. Subramaniam. Pseudo-turbulent gas-phase velocity fluctuations in homogeneous gas-solid flow: fixed particle assemblies and freely evolving suspensions. Journal of Fluid Mechanics, 770:210–246, 2015.
[40] Robert R. Nourgaliev and Theo G. Theofanous. High-fidelity interface tracking in compressible flows: unlimited anchored adaptive level set. Journal of Computational Physics, 224(2):836–866, 2007.
[41] A. Passalacqua and R. O. Fox. Implementation of an interative solution procedure for multi-fluid gas–particle flow models on unstructured grids. Powder Technology, 213(1):174–187, 2011.
[42] A. Passalacqua, J. E. Galvin, P. Vedula, C. M. Hrenya, and R. O. Fox. A quadrature-based kinetic model for dilute non-isothermal granular flows. Communications in Computational Physics, 10(01):216–252, 2011.
[43] Marica Pelanti and Randall J. LeVeque. High-resolution finite volume methods for dusty gas jets and plumes. SIAM Journal on Scientific Computing, 28(4):1335–1360, 2006.
[44] X. Rogue, G. Rodriguez, J. F. Haas, and R. Saurel. Experimental and numerical investigation of the shock-induced fluidization of a particles bed. Shock Waves, 8(1):29–45, 1998.
[45] Susana Serna and Antonio Marquina. Capturing shock waves in inelastic granular gases. Journal of Computational Physics, 209(2):787–795, 2005.
[46] G. S. Shallcross, R. O. Fox, and J. Capecelatro. A volume-filtered description of compressible particle-laden flows. International Journal of

Multiphase Flow, 122:103138, 2020.
[47] Raymond J. Spiteri and Steven J. Ruuth. A new class of optimal high-order strong-stability-preserving time discretization methods. SIAM Journal on Numerical Analysis, 40(2):469–491, 2002.
[48] Ellen M. Taylor, Minwei Wu, and M. Pino Martín. Optimization of nonlinear error for weighted essentially non-oscillatory methods in direct numerical simulations of compressible turbulence. Journal of Computational Physics, 223(1):384–397, 2007.
[49] Theo G Theofanous, Vladimir Mitkin, and Chih-Hao Chang. The dynamics of dense particle clouds subjected to shock waves. Part 1. Experiments and scaling laws. Journal of Fluid Mechanics, 792:658–681, 2016.
[50] E. F. Toro, M. Spruce, and W. Speares. Restoration of the contact surface in the HLL-Riemann solver. Shock Waves, 4(1):25–34, 1994.
[51] A. Vié, F. Doisneau, and M. Massot. On the anisotropic Gaussian velocity closure for inertial-particle laden flows. Communications in Computational Physics, 17(01):1–46, 2015.
[52] Justin L. Wagner, Kyle Daniel, Charley Downing, Thomas W. Grasser, and Kyle P. Lynch. Shock–particle-curtain interactions at high Mach number. In AIAA SCITECH 2023 Forum, page 2303, 2023.
[53] M. Wang, Y. Yang, D. Z. Zhang, and S. Balachandar. Numerical calculation of the particle–fluid–particle stress in random arrays of fixed particles. Physical Review Fluids, 6:104306, 2021.
[54] F. Zhang, D. L. Frost, P. A. Thibault, and S. B. Murray. Explosive dispersal of solid particles. Shock Waves, 10(6):431–443, 2001.